Applied Thermal Engineering 237 (2024) 121804

Contents lists available at ScienceDirect

Applied Thermal Engineering

journal homepage: www.elsevier.com/locate/apthermeng

Research Paper

Performance improvement and thermomechanical analysis of a novel asymmetrical annular thermoelectric generator

Wenlong Yang [a,b], Aoqi Xu [a], Wenchao Zhu [a,c], Yang Li [d], Ying Shi [a], Liang Huang [a], Hao Li [a], Wei Lin [a], Changjun Xie [a,b,*]

[a] School of Automation, Wuhan University of Technology, Wuhan 430070, China
[b] Hubei Key Laboratory of Advanced Technology for Automotive Components, Wuhan University of Technology, Wuhan 430070, China
[c] Hubei Key Laboratory of Fuel Cells, Wuhan University of Technology, Wuhan 430070, China
[d] Department of Electrical Engineering, Chalmers University of Technology, Gothenburg 41258, Sweden

ARTICLE INFO

Keywords:
Annular thermoelectric generator
Asymmetric structure
Impedance matching
Thermal stress

ABSTRACT

Enhancing thermoelectric performance hinges on optimizing the geometry of thermoelectric legs. In this study, we present a novel asymmetrical annular thermoelectric generator (ATEG) in which the proportions of P-type and N-type legs are meticulously balanced. We construct a one-dimensional analytical model tailored to this ATEG. Utilizing this model, we derive the relationship governing thermal-electrical impedance matching in an asymmetrical ATEG and formulate a general expression for optimizing the asymmetry coefficient. We explore the influence of various thermal boundary conditions on optimal impedance matching, ideal annular leg parameters, and the optimal asymmetry coefficient. Our findings reveal that thermal boundary conditions significantly affect the optimal load ratio. Furthermore, in comparison to traditional ATEGs, our proposed asymmetrical ATEG with the optimized structure exhibits a remarkable 16.2 % increase in output power while maintaining the same material volume. Additionally, we perform a three-dimensional numerical analysis of the asymmetrical ATEG using Comsol. Our research findings indicate that introducing the asymmetric structure leads to higher maximum thermal stress on the legs. Interestingly, the study of asymmetric thermal boundary conditions highlights that improving heat transfer between the ATEG and the cooler yields higher mechanical reliability compared to enhancing heat transfer between the ATEG and the heat source.

1. Introduction

Excessive energy consumption not only leads to energy shortages but also significantly contributes to environmental pollution, posing substantial challenges for the world. Consequently, numerous countries have set policy objectives to transition towards a low-carbon economy in response to climate change [1]. This paradigm shift has elevated the importance of energy conservation, enhancing energy conversion efficiency, and advancing renewable energy as pivotal themes in global industrial development. Moreover, the recycling and utilization of wasted energy are now seen as promising solutions, especially for industries characterized by high energy consumption during their production processes. This is because these processes typically release a substantial amount of energy into the environment as heat in the form of air or water [2]. For instance, in vehicles powered by internal combustion engines, a significant portion of fuel energy is dissipated as engine exhaust gases [3].

1.1. Literature review

Thermoelectric power generation technology is a straightforward and environmentally friendly method of converting thermal energy directly into electrical energy, eliminating the need for intermediate energy conversion units. It offers advantages such as compactness, modularity, and quiet operation. Since the dawn of the 21st century, there has been a significant surge in research interest surrounding thermoelectric generators (TEGs). In addition to their traditional applications in automobile waste heat recovery [4] and radioisotope thermoelectric recovery systems [5], TEGs are increasingly finding use in emerging and diverse fields, including wearable devices [6], photovoltaic/TEG hybrid systems [7], and autonomous sensors [8], among others. Nevertheless, thermoelectric devices grapple with the challenge of low conversion efficiency. Despite various research endeavors aimed

* Corresponding author at: School of Automation, Wuhan University of Technology, Wuhan 430070, China.
E-mail address: jackxie@whut.edu.cn (C. Xie).

https://doi.org/10.1016/j.applthermaleng.2023.121804
Received 26 July 2023; Received in revised form 9 October 2023; Accepted 16 October 2023
Available online 18 October 2023

Nomenclature

A	heat transfer area, m^2
h	heat transfer coefficient, W/(m^2•K)
h_r	ratio of heat transfer coefficient
I	current, A
k	thermal conductivity, W/(m•K)
K	thermal conductance, W/K
l	length, m
m	load ratio
n	grid number
P	power, W
q	current density, A/m^2
Q	heat flow, W
r	axial position coordinates
r_h	inner arc radius of leg, m
R	resistance, Ω
R_L	load resistance, Ω
s	Seebeck coefficient, V/K
T	temperature, K
V	voltage, V
ZT	thermoelectric figure of merit

Greek symbols

α	asymmetric parameter
δ	thickness, m
ε	calculation parameter
γ	structural parameter, m^{-1}
η	efficiency, %
$\Delta\varphi$	angle of PN legs, rad
θ	modification term
σ	Electrical conductivity, S•m
ω	thermal resistance ratio
Φ	resistance tensor

Subscripts

c	cold side
ce	ceramic
co	copper
cs	cold source
ex	external value
h	hot side
hc	hot side and cold side
hs	heat source
i	segment index
leg	a PN couple value
max	maximum value
N	N-type leg
opt	optimal value
P	P-type leg
sh	substrate of hot side
sc	substrate of cold side

Abbreviations

ATEG	annular thermoelectric generator
TEC	thermocouple
TEG	thermoelectric generator

at bolstering thermoelectric conversion capabilities, there remains substantial room for improvement before widespread commercialization becomes feasible [9]. One of the fundamental and widely applicable methods to enhance thermoelectric conversion efficiency is by improving the dimensionless figure of merit (ZT) of thermoelectric semiconductor materials [10]. The underlying principle entails elevating the material's Seebeck coefficient and electrical conductivity while simultaneously diminishing thermal conductivity. Modern synthesis and characterization techniques, such as thermoelectric modules incorporating ultrafine particles and nanoporous structures [11], as well as the production of efficient thermoelectric materials achieved by eliminating thermally conductive oxides from the surface of polycrystalline samples [12], are continuously advancing the ZT value of thermoelectric materials.

To enhance the performance of TEGs, in addition to exploring high-performance thermoelectric materials, there are three primary research directions [2]: optimizing the electrical and thermal configurations of thermoelectric modules, designing novel heat exchangers for optimization, and improving the structure of thermoelectric devices.

The power mismatch issue resulting from uneven temperature distribution among different thermoelectric modules, caused by temperature gradients, presents a significant challenge in the practical application of TEG systems [13]. In TEG systems comprising numerous TEMs, various methods exist for electrically and thermally interconnecting TEMs, including series, parallel, and mixed connections. Establishing a universal guideline for determining the optimal electrical and thermal configuration of TEMs is a pressing concern that demands attention [14]. Montecucco et al. [15] conducted a study on the impact of series or parallel electrical connections of TEMs under thermal imbalance on output power. The results revealed significant power losses due to mismatch conditions, with series connections minimizing Joule heating losses. Cózar et al. [16] investigated the influence of different electrical and thermal configurations among numerous TEMs on output power and found that mixed connections of TEMs generated higher output power compared to pure series or parallel topologies. Choi et al. [17] analyzed the trend of TEG output voltage and current with varying numbers of electrical branches and proposed an exponential fitting curve to predict the output voltage and current under different electrical branch configurations. To further mitigate power losses caused by temperature mismatch, Bijukumar et al. [18] proposed column-wise and row-wise arrangements of TEMs and demonstrated the improved performance of the column-wise arrangement through a simulated array of 5 × 5 TEMs. They also observed that the power loss in the column-wise arrangement was very close to that of the series topology, while enhancing reliability and feasibility in high-power applications.

For certain thermoelectric applications, directly installing thermoelectric modules onto heat sources can be difficult or even impossible. In such scenarios, an additional intermediate component, usually a heat exchanger, becomes necessary to capture thermal energy from the heat source and convey it to the hot side of the thermoelectric module. Therefore, the design and optimization of heat exchangers are among the important aspects that have received widespread attention in the field of thermoelectrics. Various enhanced heat transfer methods have been proposed to maximize energy extraction from the heat source.

Luo et al. [19] introduced a converging heat exchanger with its thermal side walls converging along the flow direction of the heat source. They investigated the effects of different inclinations of the heat exchanger and heat source parameters on TEG performance. The results showed a 20.2 % increase in net power for the heat exchanger with an inclination angle of 2.5° compared to the conventional TEG system. Chen et al. [20] compared the effects of no fins, plate fins, and pin fins on enhancing heat transfer and power generation of TEGs. Through simulations, they found that both plate fins and pin fins significantly improved waste heat collection in TEMs, with pin fins achieving a 24.14 % higher output power compared to plate fins. Subsequently, they

investigated the impact of the number of plate fins on the thermoelectric properties of TEGs used for low-temperature waste heat recovery at various Reynolds numbers [21]. The results indicated that although the introduction of fins increased the pressure drop within the channels, the impact was much smaller compared to the additional power generated. Meng et al. [22] designed the optimal configuration of porous pin fins installed in the flow passage of automotive exhaust heat exchangers. They employed a multi-objective optimization approach to balance the output power and exhaust pressure drop of the TEG system.

In our previous research, which focused on cylindrical heat sources and a novel annular TEG (ATEG), we proposed a concentric annular heat exchanger [23]. This heat exchanger demonstrated enhanced heat transfer performance within the cylindrical channels, resulting in a substantial increase in net power for the ATEG system. Building upon this, Zhu et al. [24] introduced a novel heat exchanger structure featuring helical twisted tapes installed in a circular exhaust pipe. They investigated the influence of various structural parameters of the helical twisted tapes on performance enhancement. The results indicated that the power and efficiency of the ATEG could be maximally increased by 10.41 % and 22.52 %, respectively, compared to a smooth exhaust pipe. In addition to the aforementioned commonly employed methods for enhancing heat transfer, innovative approaches like the utilization of foam copper [25], introduction of heat transfer fluids [26], and incorporation of heat pipes [27] have been proposed. Furthermore, besides designing more efficient heat exchangers, the utilization of phase change materials has proven to be a dependable method for maintaining relative temperature stability at the hot and cold sides [28,29].

Depending on the shape of the heat source and heat exchanger, thermoelectric devices can be designed with different structures, such as flat plate structures [3] and annular structures [23]. Geometric and structural optimization of thermoelectric devices carries significant importance, as it can diminish the amount or volume of materials needed for high-performance TEGs, thereby achieving the dual objective of enhancing thermoelectric conversion efficiency and reducing material costs. Comprehensive research has been conducted on traditional rectangular thermoelectric legs, focusing on key parameters such as cross-sectional area, leg length, and the number of legs for thermoelectric geometric optimization [13].

Furthermore, several innovative thermoelectric device structures have been developed, deviating from the traditional flat plate type. These include segmented ATEGs [30], two-stage ATEGs [31], and variable cross-sectional ATEGs [32]. Liu et al. [33] proposed a new structure that combines segmented thermoelectric materials with asymmetrical legs. In this design, the P-type legs were segmented thermoelectric materials with variable cross-sectional structures, while the N-type legs followed a conventional rectangular structure. The introduction of asymmetrical legs based on the segmented design led to a 4.21 % increase in output power. Expanding on this concept, Karana et al. [34] designed both the P-type and N-type legs as segmented materials, with the N-type legs having an exponentially varying non-uniform cross-sectional shape. Simulation results demonstrated that this structure exhibited higher output power compared to single-material configurations and conventional TEC structures. Chen et al. [35] conducted an investigation into the power generation performance and thermal stress characteristics of TEMs designed with a unileg configuration under constant temperature boundary conditions.

When applied to circular heat exchangers or heat sources, the utilization of annular thermoelectric modules offers advantages in reducing contact thermal resistance resulting from geometric mismatch [36]. Research has delved into structural optimization for annular thermoelectric legs [37] and the analysis of their mechanical and thermal stress performance [38]. Expanding on the concept of traditional rectangular TECs, segmented annular thermoelectric legs [39] and two-stage annular thermoelectric modules [40] have been proposed.

Olga et al. [41] were the first to fabricate ring TEMs using nanomaterials and implemented an annular TEG system for engine exhaust systems on a test bench. Weng et al. [42] introduced a variable-angle annular TEC and developed a one-dimensional analytical model in which the internal angle of the annular legs was determined based on an angle function. Despite a 30 % increase in maximum thermal stress, they observed a 35 % improvement in output performance for the variable-angle TEG compared to a normal ATEG. Zaher et al. [43] investigated the influence of key design parameters, including the PN leg diameter ratio, thickness ratio, and fill factor, on the thermoelectric performance of annular thermoelectric generators installed on circular heat exchangers. The objective was to enhance output performance, reduce material volume, and improve the efficiency and cost-effectiveness of ATEGs. Asaadi et al. [44] investigated the influence of structural parameters on the output power, energy conversion efficiency, and exergy efficiency of a two-stage ATEG, and compared it with a conventional single-stage ATEG. The results demonstrated that the performance of the two-stage ATEG surpassed that of the single-stage ATEG. Subsequently, Tian et al. [45] constructed a segmented ATEG by employing different thermoelectric materials on the legs, assessing the impact of its structural parameters on performance and comparing it with a standard ATEG. They found that the segmented structure exhibited superior power generation performance and cost-effectiveness. The asymmetry in these studies is manifested in the variation of cross-sectional areas along the height direction of the thermoelectric legs, with most studies treating the structures of P-type and N-type thermoelectric legs as identical.

1.2. Motivation and innovation

In view of the reviewed works, due to their structural advantages, ATEGs may prove more suitable for large-scale production and integration with tubular heat exchangers, a trend that has increasingly garnered significant interest. Under common thermal boundary conditions, for a typical TEG, increasing the length of the thermoelectric legs simultaneously results in an increase in internal resistance and a decrease in thermal conductance. These two phenomena exert opposing influences on thermoelectric performance, creating a need for a compromise in leg height. This compromise allows resistance and thermal conductance to strike a balance, thereby maximizing thermoelectric performance. Likewise, modifying the cross-sectional area of the legs triggers inverse changes in resistance and thermal conductance. Previous studies have usually assumed identical structures for P-type and N-type support legs, conducting compromise optimizations between the physical properties of thermoelectric semiconductors and their geometric structures [35,36]. However, due to differences in material properties, P-type and N-type support legs each possess an optimal geometric structure capable of individually achieving optimal values of resistance and thermal conductance on the legs. This individual optimization approach serves to maximize thermoelectric performance [46].

Previous research on asymmetrical TEGs has often involved different geometric configurations. For example, P-type legs were conventionally designed as rectangles, whereas N-type legs took the form of segmented structures, trapezoidal structures [33], or structures with exponentially varying cross-sectional areas [34]. However, theoretically, the shape of thermoelectric legs can be designed arbitrarily, resulting in a multitude of different P-N combinations. Optimizing such a vast array of asymmetric geometric designs is inefficient. This study is based on the premise of configuring both P-type and N-type legs as annular-shaped support legs and subsequently optimizing the size ratio of P-type to N-type legs. Currently, there is a lack of universal design guidelines to assist in the geometric optimization of asymmetrical ATEGs.

Furthermore, the existing research on TEGs has primarily focused on investigations assuming an internal-to-external load ratio of 1. It has been observed that the load resistance at maximum output power exceeds the internal resistance of the TEM [47], and impedance matching models have been developed for flat TECs [48]. However, the applicability of these findings to annular structures has not yet been validated.

Moreover, there is a scarcity of research concerning the thermal reliability and thermomechanical properties for asymmetrical ATEGs under 3D modeling and analysis.

1.3. Overview of research content

In summary, the purpose of this study is to address the limitations of previous research, which made unreasonable assumptions such as equal internal and external loads and identical structures for P-type and N-type legs. The objective is to gain a comprehensive understanding of the optimal thermoelectric performance of asymmetrical legs when thermoelectric impedance is matched. Furthermore, the study aims to investigate the impact of different thermal boundary conditions on the mechanical reliability of asymmetrical leg structures and provide valuable design guidance for future studies on ATEGs. To achieve these goals, several steps will be taken. Firstly, a comprehensive analytical model for ATEGs will be developed, allowing the derivation of expressions for thermal-electric impedance matching conditions and optimal parameters of asymmetric structures. Subsequently, the impact of different thermal boundary conditions on the optimal impedance matching conditions, optimal annular structure parameters, and optimal asymmetry coefficients of ATEGs will be investigated. Finally, three-dimensional simulations will be conducted using COMSOL software to analyze the electric potential distribution, temperature distribution, and thermal stress distribution of asymmetrical ATEGs. Overall, the study aims to provide a deeper understanding of the performance and reliability of asymmetrical ATEGs and contribute valuable design guidelines for future research in this field.

2. Model and mathematical formulation description

A ring-shaped thermoelectric module, used for power generation, consists of multiple pairs of annular thermoelectric couples. Each annular thermoelectric couple, as shown in Fig. 1(a), comprises thermoelectric legs and a substrate layer. To accommodate a cylindrical heat source, the upper and lower walls of the thermoelectric couple are curved. Copper connecting strips, bent to the same curvature, connect the P-type and N-type semiconductor elements within each thermoelectric couple. Curved ceramic layers cover the upper and lower walls of the semiconductor legs. When a temperature gradient ΔT_{leg} is applied across the ATEG, the charge carriers within the semiconductor diffuse from the hot end with higher concentration to the cold end with lower concentration. This diffusion process leads to the generation of positive and negative charges at the respective hot and cold ends, thereby creating an electrostatic field. As the diffusion and drift motions of the charge carriers reach an equilibrium state, thermal energy is converted into electrical energy. When a load is connected, the electrical energy is output from the thermoelectric legs in the form of current. In constructing the theoretical model, we neglect thermal convection and thermal radiation on the lateral surfaces of the thermoelectric legs, as well as the contact thermal resistance and contact electrical resistance at the junction points.

2.1. Basic equations

Based on the constitutive relationship between the motion of charge carriers and heat transfer within the thermoelectric semiconductor, the thermal flux $\boldsymbol{q}_T$ and current density $\boldsymbol{q}_V$ of the thermoelectric field can be expressed using the governing equations:

$$\begin{cases} \boldsymbol{q}_V = -\sigma\nabla V - \sigma s\nabla T \\ \boldsymbol{q}_T = sT\boldsymbol{q}_V - k\nabla T \end{cases} \tag{1}$$

Here, V and T represent the electric potential and temperature, respectively, while σ, s, and k represent the electric conductivity, Seebeck coefficient, and thermal conductivity of the semiconductor elements, respectively.

The thermoelectric coupling equations are given by

$$\begin{cases} \nabla\boldsymbol{q}_V = 0 \\ \nabla\boldsymbol{q}_E = 0 \end{cases} \tag{2}$$

Where, $\boldsymbol{q}_E = \boldsymbol{q}_T + V\boldsymbol{q}_V$ is the energy flux. The divergence of $V\boldsymbol{q}_V$ stands for Joule heat. According to Eq. (2), $\boldsymbol{q}_E$ is divergence-free, while $\boldsymbol{q}_T$ is not.

The relationship between electric flux, energy flux, temperature gradient, and electric potential gradient can be expressed by the conduction tensor Φ [48].

$$\begin{cases} \boldsymbol{q}_V = -(\Phi_{VV}\nabla V + \Phi_{VT}\nabla T) \\ \boldsymbol{q}_E = -(\Phi_{TV}\nabla V + \Phi_{TT}\nabla T) \end{cases} \tag{3}$$

$$\Phi = \begin{pmatrix} \sigma & s\sigma \\ V\sigma + s\sigma T & k + s\sigma V + s^2\sigma T \end{pmatrix} \tag{4}$$

2.2. Theoretical model

As shown in Fig. 1(b), the ATEG is divided into n computational units, where r_i represents the radius of the i-th unit, and $r_0 = r_h$, $r_n = r_h + l_{leg}$. Based on the established physical model and model assumptions, the current flux and energy flux in the radial direction are conserved. For the i-th discrete unit in a thermoelectric leg (indicated by subscript χ for P or N), Eq. (3) can also be expressed as

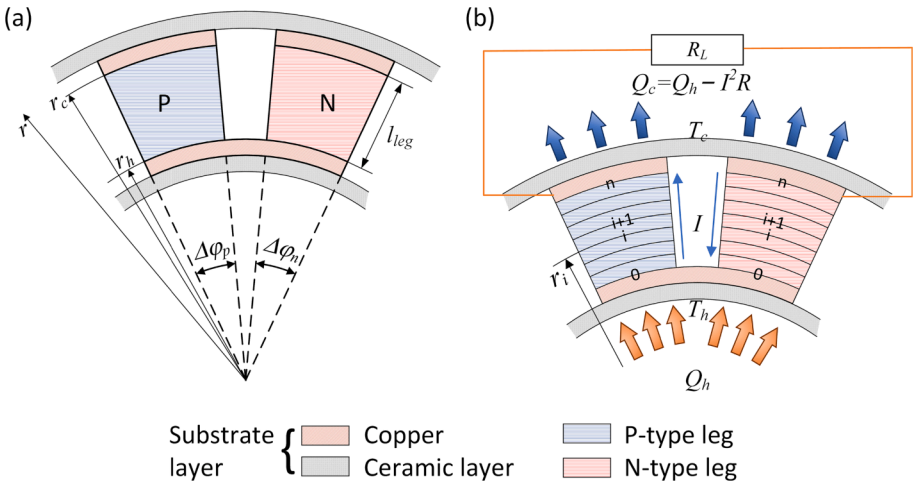

Fig. 1. (a) Schematic diagram of structural parameters and (b) physical model of an ATEG.

$$\begin{pmatrix} V_{\chi,i+1}-V_{\chi,i} \\ T_{\chi,i+1}-T_{\chi,i} \end{pmatrix} = -\frac{\ln(r_{i+1}/r_i)}{\Delta\varphi_\chi\delta_\chi}\Phi^{-1}_{\chi,i+1/2}\begin{pmatrix} I_\chi \\ Q_\chi \end{pmatrix} \tag{5}$$

Where $\Phi^{-1}_{\chi,i+1/2}$ denotes the impedance tensor of the i-th unit, which is the inverse of the matrix Φ and is expressed as

$$\Phi^{-1}_{\chi,i+1/2} = \begin{pmatrix} \sigma^{-1}+s^2k^{-1}V+sk^{-1}T & -sk^{-1} \\ -sk^{-1}T-k^{-1}V & k^{-1} \end{pmatrix}_{\chi,i+1/2} \tag{6}$$

The temperature and potential of each unit are represented by the arithmetic average of the i-th and $(i+1)$-th computational units, that is, $V_{\chi,i+1/2}=(V_{\chi,i}+V_{\chi,i+1})$,$T_{\chi,i+1/2}=(T_{\chi,i}+T_{\chi,i+1})$. Additionally, σ, s, and k are highly dependent on $T_{\chi,i+1/2}$. Therefore, Eq. (5) can also be expressed as

$$\begin{pmatrix} V_{\chi,n}-V_{\chi,0} \\ T_{\chi,n}-T_{\chi,0} \end{pmatrix} = -\alpha_\chi\overline{\Phi}_\chi^{-1}\begin{pmatrix} I_\chi \\ Q_\chi \end{pmatrix}, \overline{\Phi}_\chi^{-1} = \frac{1}{n}\sum_{i=0}^{n-1}\Phi^{-1}_{\chi,i+1/2} \tag{7}$$

Where α_χ represents the structural parameter of the annular leg:

$$\alpha_\chi = \int_{r_h}^{r_h+l_{leg}}\frac{1}{A_\chi(r)}dr = \sum_{i=0}^{n-1}\frac{\ln(r_{i+1}/r_i)}{\Delta\varphi_\chi\delta_\chi} = \frac{\ln[(r_h+l_{leg})/r_h]}{\Delta\varphi_\chi\delta_\chi} \tag{8}$$

According to the ATEG model proposed in Fig. 1, the lengths of the P-type and N-type legs should be equal, i.e., $l_{leg}=l_P=l_N$. Under the constraint of maintaining the overall volume of a single ATEG, α_P and α_N are parameters to be optimized. We define $\gamma=\alpha_P/\alpha_N$, which represents the ratio between the structural parameters of the P-type and N-type legs and characterizes the degree of asymmetry in the asymmetrical ATEG. Fig. 2 illustrates the schematic diagram of ATEG's geometric structure for different γ values. Here, $\gamma<1$ indicates that the N-type leg is thinner than the P-type leg, while $\gamma>1$ indicates the opposite. $\gamma=1$ represents the conventional symmetrical ATEG.

For the contact points of the theoretical model, assuming $T_{N,0}=T_{P,0}$, $V_{P,0}=V_{N,0}=0$, the thermal-electric field can be calculated as follows

$$\overline{\Phi}_{\chi,VV}(V_{\chi,0}-V_{\chi,n})+\overline{\Phi}_{\chi,VT}(T_{\chi,0}-T_{\chi,n})=\alpha_\chi I_\chi \tag{9a}$$

$$\overline{\Phi}_{\chi,TV}(V_{\chi,0}-V_{\chi,n})+\overline{\Phi}_{\chi,TT}(T_{\chi,0}-T_{\chi,n})=\alpha_\chi Q_\chi \tag{9b}$$

The current directions on the P-type leg and N-type leg are opposite. After connecting the load, it satisfies $V_{P,n}-V_{N,n}=IR_L$, where the series current I is calculated as

$$I=\frac{\Delta T_{leg}(\overline{\Phi}^{-1}_{P,VV}\overline{\Phi}^{-1}_{P,VT}-\overline{\Phi}^{-1}_{N,VV}\overline{\Phi}^{-1}_{N,VT})}{\alpha_P\overline{\Phi}^{-1}_{P,VV}+\alpha_N\overline{\Phi}^{-1}_{N,VV}+R_L} \tag{10}$$

Where $\Delta T_{leg}=T_{\chi,0}-T_{\chi,n}$. According to Eq. (9b), the thermal flux at the hot end of the P-type leg and N-type leg can be expressed as

$$\begin{cases} Q_P=\Delta T_{leg}(\overline{\Phi}_{P,TT}-\overline{\Phi}_{P,VT}\overline{\Phi}_{P,TV}\overline{\Phi}^{-1}_{P,VV})/\alpha_P+I\overline{\Phi}_{P,TV}\overline{\Phi}^{-1}_{P,VV} \\ Q_N=\Delta T_{leg}(\overline{\Phi}_{N,TT}-\overline{\Phi}_{N,VT}\overline{\Phi}_{N,TV}\overline{\Phi}^{-1}_{N,VV})/\alpha_N-I\overline{\Phi}_{N,TV}\overline{\Phi}^{-1}_{N,VV} \end{cases} \tag{11}$$

According to Eqs. (4) and (11), the ZT value, average temperature, equivalent electrical resistance, equivalent thermal conductivity, and equivalent Seebeck coefficient of an ATEG can be calculated as follows

$$\begin{cases} T_{leg}=(\overline{\Phi}^{-1}_{P,VV}\overline{\Phi}_{P,TV}-\overline{\Phi}^{-1}_{N,VV}\overline{\Phi}_{N,TV})(\overline{\Phi}^{-1}_{P,VV}\overline{\Phi}_{P,VT}-\overline{\Phi}^{-1}_{N,VV}\overline{\Phi}_{N,VT})^{-1} \\ R_{leg}=\alpha_P/\overline{\sigma}_P+\alpha_N/\overline{\sigma}_N=\alpha_P\overline{\Phi}^{-1}_{P,VV}+\alpha_P\overline{\Phi}^{-1}_{N,VV} \\ K_{leg}=\overline{k}_P/\alpha_P+\overline{k}_N/\alpha_N=\sum_{\chi=P,N}(\overline{\Phi}_{\chi,TT}-\overline{\Phi}_{\chi,VT}\overline{\Phi}_{\chi,TV}\overline{\Phi}^{-1}_{\chi,VV})/\alpha_\chi \\ S=\overline{\Phi}^{-1}_{P,VV}\overline{\Phi}_{P,VT}-\overline{\Phi}^{-1}_{N,VV}\overline{\Phi}_{N,VT} \\ ZT=S(\overline{\Phi}^{-1}_{P,VV}\overline{\Phi}_{P,TV}-\overline{\Phi}^{-1}_{N,VV}\overline{\Phi}_{N,TV})/RK \end{cases} \tag{12}$$

When applying convective boundary conditions on both sides of the ATEG, the thermal resistances at the hot end (K_h^{-1}) and the cold end (K_c^{-1}) are given by [37]

$$K_h^{-1}=A_{sh}^{-1}/h_h+\ln[r_h/(r_h-l_{co})]/k_{co}+\ln[(r_h-l_{co})/(r_h-l_{co}-l_{ce})]/k_{ce} \tag{13a}$$

$$K_c^{-1}=A_{sc}^{-1}/h_c+\ln[(r_h+l_{co})/r_h]/k_{co}+\ln[(r_h+l_{co}+l_{ce})/(r_h+l_{co})]/k_{ce} \tag{13b}$$

Next, the output performance of an ATEG can be calculated using the aforementioned explicit expressions. Based on energy conservation, we can obtain

$$Q_h=Q_P+Q_N=K_h(T_{hs}-T_{\chi,0})=K_c(T_{\chi,n}-T_{cs})+P \tag{14}$$

Where the output power of the ATEG is defined as $P=I^2R_L$. We introduce the following definition:

$$\begin{cases} m=R_L/R_{leg} \\ \omega=K_{leg}K_{ex}^{-1} \end{cases} \tag{15}$$

Where K_{ex}^{-1} represents the external thermal resistance, defined as $K_{ex}^{-1}=K_h^{-1}+(1-\eta)K_c^{-1}$, and conversion efficiency η is calculated as $\eta=P/Q_h$. By combining Eqs. (10)–(12) and (14), we can obtain

$$\begin{cases} \Delta T_{leg}=\dfrac{(m+1)\Delta T_{hc}}{\omega(ZT+m+1)+m+1} \\ I=\dfrac{S\Delta T_{hc}}{R_{leg}[\omega(ZT+m+1)+m+1]} \\ Q_h=\dfrac{K_{leg}(ZT+m+1)\Delta T_{hc}}{\omega(ZT+m+1)+m+1} \end{cases} \tag{16}$$

It is worth noting that when h_h and h_c approach infinity, it can be regarded as the isothermal boundary condition for ATEG. In this case, P and η can be explicitly expressed as:

$$P=\frac{mK_{leg}\Delta T_{hc}^2ZT}{T_{leg}[\omega(ZT+m+1)+m+1]^2} \tag{17}$$

$$\eta=\frac{m\Delta T_{hc}ZT}{T_{leg}(ZT+m+1)[\omega(ZT+m+1)+m+1]} \tag{18}$$

Due to the mismatch between thermal resistance and electrical resistance, it has been reported that the load resistance at maximum output power is higher than the internal resistance [47]. The condition for thermal-electrical impedance matching varies depending on the thermal source parameters and the structure of the thermoelectric

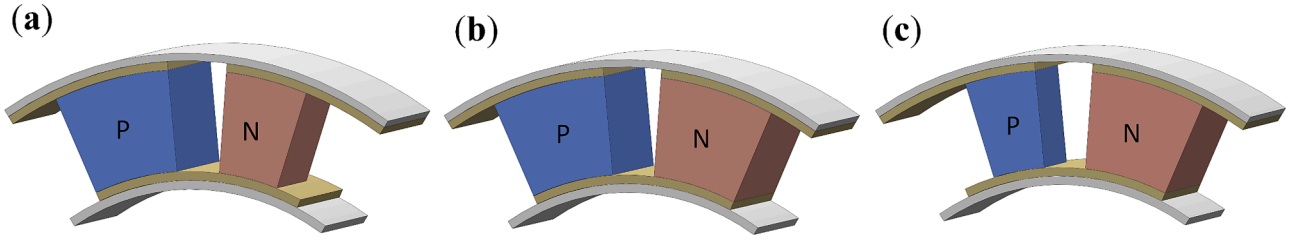

Fig. 2. Schematic diagram of asymmetrical ATEGs for different γ: (a) $\gamma<1$; (b) $\gamma=1$; (c) $\gamma>1$.

elements. Here, by deriving the partial derivative of ln$P$ with respect to m, explicit expressions for the optimal load ratio and maximum output power can be obtained [48]:

$$m(P_{\max}) = \frac{\omega ZT + \omega + 1}{\omega + 1} + \varepsilon_{po} \tag{19a}$$

$$P_{\max} = f_{p_{\max}}(\varepsilon_{po}) \frac{K \Delta T_{hc}^2 ZT}{4T_{leg}(\omega ZT + \omega + 1)(\omega + 1)} \tag{19b}$$

Similarly, the explicit expressions for the optimal load ratio $m(\eta_{\max})$ at maximum conversion efficiency $\eta_{\max}$ can be derived as [48]:

$$m(\eta_{\max}) = \sqrt{\frac{(\omega ZT + \omega + 1)(1 + ZT)}{\omega + 1}} + \varepsilon_{\eta} \tag{20a}$$

$$\eta_{\max} = \frac{1}{T_{leg}} \cdot \frac{\Delta T_{hc} ZT}{[\sqrt{\omega ZT + \omega + 1} + \sqrt{(\omega + 1)(ZT + 1)}]^2 + f_{\eta_{\max}}(\varepsilon_{\eta})} \tag{20b}$$

$$\begin{cases} \varepsilon_{PO} = (m^2 + m + \dfrac{ZT\omega}{\omega + 1}) \dfrac{\partial \ln(K_{leg} ZT / T_{leg})}{\partial m} - \dfrac{2m}{\omega + 1}(\omega \dfrac{\partial ZT}{\partial m} + \beta \dfrac{\partial \omega}{\partial m}) \\ f_{p_{\max}}(\varepsilon_{PO}) = \dfrac{1 + \varepsilon_{P_{\max}} / m(P_{\max})|_{\varepsilon_{PO}=0}}{[1 + 0.5\varepsilon_{P_{\max}} / m(P_{\max})|_{\varepsilon_{PO}=0}]^2} \\ \varepsilon_{\eta} = \dfrac{m\beta(\beta\omega + m + 1)}{\omega + 1} \dfrac{\partial \ln(ZT / T_{leg})}{\partial m} - \dfrac{m}{\omega + 1}[(2\beta\omega + m + 1) \dfrac{\partial ZT}{\partial m} + \beta^2 \dfrac{\partial \omega}{\partial m}] \\ f_{\eta_{\max}}(\varepsilon_{\eta}) = \dfrac{(\omega + 1) m(\eta_{\max})}{[1 - m(\eta_{\max})|_{\varepsilon_{\eta}=0} / m(\eta_{\max})]^2} \end{cases} \tag{21}$$

Where $\beta = ZT + m + 1$, ε and $f(\varepsilon)$ are parameters used to account for the effects of errors in the equivalent temperature and thermal resistance on the optimal load ratio in Eqs. (19) and (20). When this influence is negligible, i.e., ε approaches 0, $f_{Pmax}(\varepsilon_{PO}) = 1$ and $f_{\eta max}(\varepsilon_{\eta}) = 0$.

2.3. Boundary conditions

In this study, the boundary conditions for the ATEG can be categorized as isothermal and convective heat exchange conditions. When h approaches infinity, the convective thermal resistance becomes negligible, resulting in an isothermal condition where heat conduction from the hot end to the cold end becomes the dominant mode of heat transfer. When a specific value of h is defined, it is considered a convective heat transfer condition. Alternatively, by setting h_h to infinity and assigning a specific value to h_c, one can establish a condition where the hot end is isothermal, and a convective boundary condition is applied to the cold end.

2.4. Solution process

The temperature distribution, voltage distribution, and output characteristics of the ATEG can be obtained quickly and accurately by iteratively solving Eqs. (5) and (12)–(16). The solution process flowchart of this nonlinear theoretical model for the thermal-electric field is illustrated in Fig. 3.

Firstly, the initial structural parameters of the PN legs are determined, and the boundary conditions are set. Secondly, in each iteration process, the three key parameters in Eq. (16) are calculated using Eqs. (11) and (12), and then substituted into Eq. (5) to obtain the temperature and voltage distribution. Next, the equivalent parameters of the PN legs are calculated using the updated thermal-electric field, and the power and efficiency are computed. This iteration process is repeated until the desired level of model accuracy is achieved. The structural parameters and properties of the substrate layer are fixed, while the initial values of parameters such as l_{leg}, r_h, $\Delta\varphi_\chi$, and δ_χ, which influence the asymmetrical ATEG structure, are listed in Table 1. BiTe-Based N-type nanocomposite thermoelectric materials [49] and P-type bismuth antimony telluride materials (Bi-Sb-Te) [50] were chosen, which exhibit highly temperature-dependent properties. The fitting expressions for their thermal-electric properties are shown in Table 2.

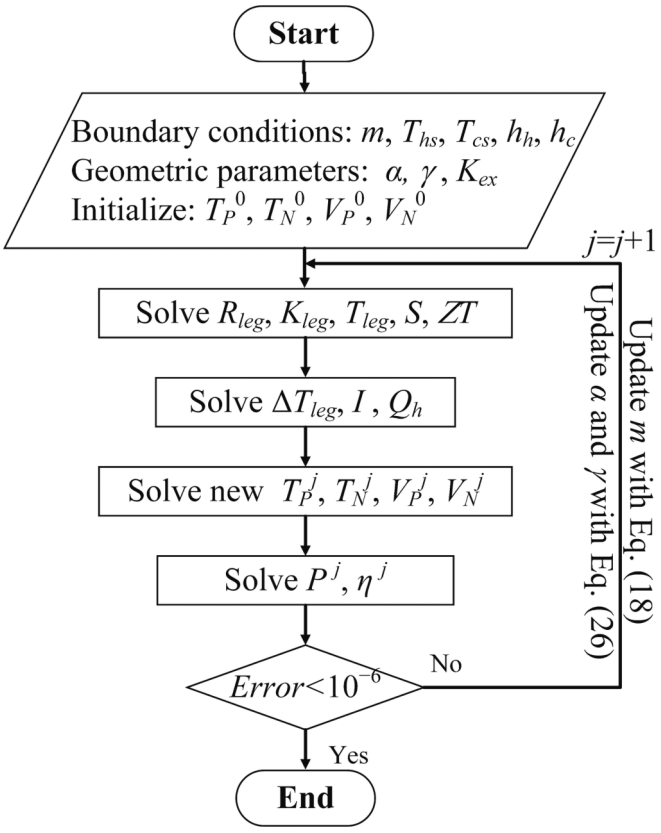

Fig. 3. Solution process schedule of the theoretical model.

Table 1
Initial structure characteristics of the ATEG.

Parameter	Value	Units
Thickness of ceramic sheet, l_{ce}	0.001	m
Thickness of conductive plate, l_{co}	0.0005	m
Substrate area of hot side, A_{sh}	4.359×10^{-6}	m^2
Substrate area of cold side, A_{sc}	5.066×10^{-6}	m^2
Height of thermoelectric legs, l_{leg}	0.003	m
Thickness of thermoelectric legs, δ_χ	0.0015	m
Angle of thermoelectric legs, $\Delta\varphi_\chi$	0.0698	rad
Radius of ATEG hot side, r_h	0.02	m

Eqs. (19) and (20) provide the expressions for the optimal load ratio, aiming to maximize P and η, respectively. These equations are the thermal-electrical impedance matching equations of ATEG. This model is developed as an improved version based on the one-dimensional self-consistent flat-plate TEG model derived by He et al. [48]. To improve the accuracy of the impedance matching equations, a correction parameter is introduced using Eq. (21). However, it is worth noting that even without the correction parameter ($\varepsilon = 0$), the model can achieve significant accuracy and computational efficiency. This thermoelectric model and the impedance matching equations achieve self-consistency by considering the temperature dependence of thermoelectric semiconductors and incorporating nearly all thermoelectric effects, including the Thomson effect.

2.5. Structural optimization of asymmetrical ATEG

According to Eqs. (12) and (19)–(20), it is observed that by altering the structural parameters of the legs, specifically affecting the K_{leg}, R_{leg},

Table 2
Physical properties of the ATEG.

Component	Material	Property	Value	Units
Substrate	Ceramic	Thermal conductivity, k_{ce}	35	W/(m·K)
	Copper	Thermal conductivity, k_{co}	398	W/(m·K)
P-type leg	Bi-Sb-Te [49]	Seebeck coefficient, s_P	$7.4634\times10^{-8}T^4 - 1.114\times10^{-4}T^3 + 0.0579\,T^2 - 12.315\,T + 1120.68925$	μV/K
		Resistivity, $\sigma_P{}^{-1}$	$8.528\times10^{-9}T^4 - 1.3889\times10^{-5}T^3 + 0.00826\,T^2 - 2.0514\,T + 191.7808$	μΩ·m
		Thermal conductivity, k_P	$4.497\times10^{-10}T^4 - 7.34\times10^{-7}T^3 + 4.599\times10^{-4}T^2 - 0.1285\,T + 14.017$	W/(m·K)
N-type leg	Bi-Te [48]	Seebeck coefficient, s_N	$2.463\times10^{-8}T^4 - 4.3588\times10^{-5}T^3 + 0.0296\,T^2 - 9.0956\,T + 863.8895$	μV/K
		Resistivity, $\sigma_N{}^{-1}$	$-4.374\times10^{-10}T^4 + 6.0927\times10^{-7}T^3 - 3.6679\times10^{-4}T^2 + 0.1383\,T - 12.63725$	μΩ·m
		Thermal conductivity, k_N	$-4.2933\times10^{-10}T^4 + 7.2296\times10^{-7}T^3 - 4.39729\times10^{-4}T^2 + 0.1153\,T - 9.9355$	W/(m·K)

and ZT of the ATEG, the output performance can be further influenced. The equivalent Seebeck coefficient of the thermoelectric semiconductor are not affected by α_χ. Taking the P-type leg as an example and assuming a fixed substrate area, based on Eqs. (19) and (20), the optimal structural parameters for maximum power and maximum efficiency can be derived by assuming $\partial \ln P_{max}/\partial\alpha_P = 0$ and $\partial \ln \eta_{max}/\partial\alpha_P = 0$, respectively:

$$\begin{cases} \alpha_P^2(P_{\max}) = \dfrac{R_{leg}(ZT\omega^2+2\omega^2+2\omega)}{K_{leg}(\omega+1)^2}\dfrac{k_P + k_N\alpha_P^2\alpha_N^{-2}\dfrac{\partial\alpha_N}{\partial\alpha_P}}{\sigma_P^{-1}+\sigma_N^{-1}\dfrac{\partial\alpha_N}{\partial\alpha_P}} \\ \alpha_P^2(\eta_{\max}) = \dfrac{R_{leg}(ZT\omega+2\omega+1)}{K_{leg}(\omega+1)}\dfrac{k_P + k_N\alpha_P^2\alpha_N^{-2}\dfrac{\partial\alpha_N}{\partial\alpha_P}}{\sigma_P^{-1}+\sigma_N^{-1}\dfrac{\partial\alpha_N}{\partial\alpha_P}} \end{cases} \tag{22}$$

Given the fixed values of l_{leg} and r_h, the optimization of α_χ requires the independent selection of values for $\Delta\varphi_\chi$ and δ_χ. In previous studies, these values were empirically designed within certain ranges and scanned to obtain the optimal parameters. However, without additional constraints, it can be challenging to determine these optimal parameters individually, particularly in the case of asymmetrical ATEGs.

With the assumption of a predetermined γ, and by setting $\alpha = \alpha_P = \gamma\alpha_N$, we have $\partial\alpha_N/\partial\alpha_P = \gamma^{-1}$. Eq. (22) can be simplified as follows:

$$\begin{cases} \alpha_{opt}(P_{\max}) = K_{ex}^{-1}(k_P+\gamma k_N)\sqrt{1+ZT} \\ m(P_{\max}) = \sqrt{1+ZT}\,,\ \omega = \dfrac{1}{\sqrt{1+ZT}} \\ P_{\max} = \dfrac{\Delta T_{hc}^2 K_{leg} ZT}{4T_{leg}(\sqrt{1+ZT}+1)^2} \\ \eta(P_{\max}) = \dfrac{\Delta T_{hc} ZT}{2T_{leg}(\sqrt{1+ZT}+1)^2} \end{cases} \tag{23}$$

The equation above provides the optimal structural parameters α, optimal load ratio, and maximum output power for a given γ. However, it does not determine the optimal values of l_{leg}, $\Delta\varphi_\chi$, and δ_χ. If we assume a fixed total volume for a pair of PN legs, that is, ${\alpha_P}^{-1} + {\alpha_N}^{-1} = \text{const}$, and optimize with respect to γ, we have $\partial\alpha_N/\partial\alpha_P = -\gamma^{-2}$. Consequently, Eq. (22) can be expressed as

$$\begin{cases} \gamma_{opt}(P_{\max}) = (\sqrt{4\sigma_P\sigma_N^{-1}+\theta_{PO}^2}+\theta_{PO})/2 \\ \gamma_{opt}(\eta_{\max}) = (\sqrt{4\sigma_P\sigma_N^{-1}+\theta_\eta^2}+\theta_\eta)/2 \end{cases} \tag{24}$$

Where θ_{PO} and θ_η are the parameter terms, and they are defined as

$$\begin{cases} \theta_{PO} = (k_P k_N^{-1}-1)\dfrac{\gamma_{opt}+\sigma_P\sigma_N^{-1}}{\gamma_{opt}+k_P k_N^{-1}}\dfrac{ZT\omega^2+2\omega^2+2\omega}{(\omega+1)^2} \\ \theta_\eta = (k_P k_N^{-1}-1)\dfrac{\gamma_{opt}+\sigma_P\sigma_N^{-1}}{\gamma_{opt}+k_P k_N^{-1}}\dfrac{ZT\omega+2\omega+1}{\omega+1} \end{cases} \tag{25}$$

The aforementioned optimal asymmetric parameter γ_{opt} can be obtained through a straightforward fixed-point iteration using the mathematical model described in Section 2.2 and Fig. 3. The process starts by assigning an initial value to γ, which is then substituted into Eq. (25). The new γ is calculated using Eq. (24) and compared with the initial γ. This process is repeated, using the new γ as the initial value for the next iteration, until the two γ values are equal.

To simultaneously determine the optimal values of γ and α, Eqs. (23) and (24) can be combined, yielding the following expressions for the structural parameters at maximum power point:

$$\begin{cases} \alpha_{opt}(P_{\max}) = K_{ex}^{-1}(k_P+\gamma k_N)\sqrt{1+ZT} \\ \gamma_{opt}(P_{\max}) = (\sqrt{\theta^2+4\sigma_P\sigma_N^{-1}}+\theta)/2 \end{cases} \tag{26}$$

$$\theta = (k_P k_N^{-1}-1)\frac{\gamma_{opt}+\sigma_P\sigma_N^{-1}}{\gamma_{opt}+k_P k_N^{-1}} \tag{27}$$

Eqs. (19), (20), and (26) constitute a comprehensive design methodology that facilitates the thermal-electrical impedance matching of ATEGs across a range of thermal-electric materials and configurations. This approach offers a way to determine the optimal structural parameters of asymmetrical ATEGs, taking into account the specific properties of P- and N-type materials, and accounting for various external impedance conditions.

3. Model validation

The analytical model was validated by comparing it with a three-dimensional numerical model constructed in Comsol. For the validation, r_h was set to 20 mm and l_{leg} was set to 3 mm. Under constant temperature boundary conditions, the cold-side temperature was fixed at 300 K, while the hot-side temperature was set at 400 K and 500 K, respectively. For the convective boundary conditions, T_{hs} was set to 500 K, T_{cs} was set to 300 K, and $h_h = h_c = h$. The temperature difference between the heat source and the cold source, represented by ΔT_{hc}, was defined as $\Delta T_{hc} = T_{hs} - T_{cs}$. The Comsol software was used for finite element analysis, and the circuit interface was utilized to connect the load resistance. At the cold end of the N-type leg, a zero potential was applied to the copper plate, while at the cold end of the P-type leg, a terminal was connected to the load resistance. Thermoelectric performance curves were obtained using both the analytical model and the Comsol model under different boundary conditions. The models were set with identical structural parameters, material properties, and boundary conditions. Fig. 4(a) and (b) illustrate the R_L-P and R_L-η curves, respectively, under constant temperature and convective boundary conditions. A comparison of the curves shows a high level of consistency between the output characteristics predicted by the two models. The maximum deviation between the models, for different load resistances, was 1.4 %. This confirms the accuracy of the analytical model.

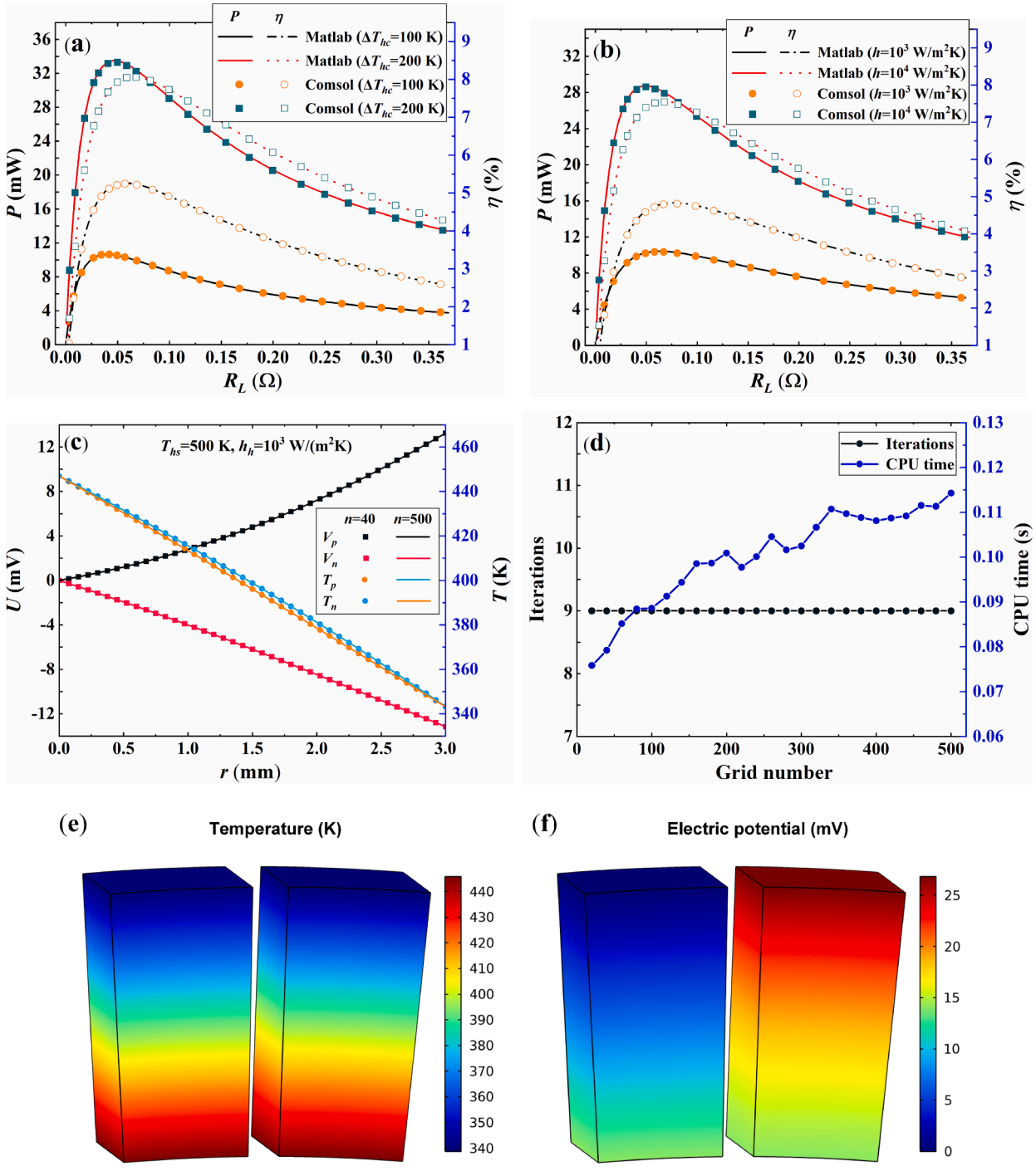

Fig. 4. Model validation of the present model with 3D model for (a) constant temperature boundary conditions and (b) convective boundary conditions; (c) Grid independence examination and (d) the model operational efficiency; (e) Temperature field and (f) potential field distribution in Comsol.

To examine the grid independence of the model, simulations were conducted with two different grid quantities, i.e., $n = 40$ and $n = 500$. Fig. 4(c) depicts the temperature and voltage distributions of the ATEG for the two grid quantities. It can be observed that the thermal-electric field distributions exhibit a high degree of similarity regardless of the grid quantity. The relative error between the two grids is less than 1 %.

Furthermore, Fig. 4(d) shows the model iteration count and CPU time for the different grid quantities. The iteration count remains consistent regardless of the grid quantity, indicating the analytical model's superlinear convergence. The CPU time increases with the grid quantity but remains below 10e−3 for a sufficiently accurate model. This is not only significantly better than three-dimensional simulation methods but also more efficient than the one-dimensional mathematical model proposed in [42]. The analytical model achieves satisfactory accuracy and computational efficiency with $n = 40$. Fig. 4(e) and (f) illustrate the thermal and electric field distributions obtained from the three-dimensional model constructed in Comsol, using the same model parameters as in Fig. 4(c). A comparison reveals a high degree of similarity between the thermal-electric fields of the three-dimensional model and the analytical model.

Additionally, the model's validity was further confirmed by comparing it with experimental data from Ebling et al. [51]. In Ref. [51],

the rectangular TEC can be considered as a special case with rh approaching infinity when compared to the physical model proposed in this study. The dimensions of the TEC in the reference are 1.5 mm × 1.5 mm × 10 mm. The same constant temperature conditions for the cold and hot sides (T_{cs} = 300 K) were applied, and the internal and external load resistances were matched. Fig. 5 presents the validation results of the output voltage for different temperature differentials. It can be observed that the maximum error between the experimental results and the computational results obtained from this model is less than 2 %, indicating that the model effectively reproduces the experimental findings. The enhanced accuracy of this model is primarily attributed to the consideration of the Thomson effect. When the Thomson effect is omitted, the heat flow at the hot end of the ATEG is overestimated, whereas the heat flow at the cold end is underestimated. Consequently, the output power predicted by this model is lower than that predicted in Ref. [51]. As suggested by Asaadi et al. [52], the Thomson effect influences the current, voltage, efficiency, and power of the TEG, resulting in their reduction. These results provide an evidence of the model's validity and reliability, allowing for further analysis and investigation.

4. Results and discussion

4.1. Thermoelectric impedance matching

Two key performance metrics, i.e., output power and conversion efficiency, are widely used to assess the effectiveness of a TEG. However, optimizing both of these metrics simultaneously for a specific TEG can be a challenging task [53]. Previous research studies have adopted various performance metrics to optimize TEGs, but most of them have relied on the assumption of internal and external load are equal. Nevertheless, it should be noted that the optimal performance and impedance matching conditions of a TEG are heavily influenced by factors such as thermoelectric material properties, thermal boundary conditions, and electrical characteristics. In this section, our objective is to explore the thermal and electrical impedance matching conditions of the ATEG under different boundary conditions, with the aim of achieving maximum power output and conversion efficiency. By doing so, we aim to shed light on the unrealistic assumptions that have been made in previous literature and provide a clearer understanding of this aspect.

4.1.1. Constant temperature boundary condition

The first step involves evaluating the electrical performance of a symmetrical ATEG. This is done by obtaining *U-I*, *P-I*, and *η-I* curves of the ATEG while varying the load resistance at different temperature differentials, as shown in Fig. 6(a) and (b). Additionally, another approach is employed to determine the optimal load ratio, referred to as "m_{opt}", by iteratively updating it using equations (19a) and (20a) with the specified boundary conditions. As depicted in the figures, the optimal load ratio derived from the mathematical expressions closely matches the one obtained through numerical methods, indicating that Eqs. (19) and (20) accurately estimate the load matching conditions of the ATEG.

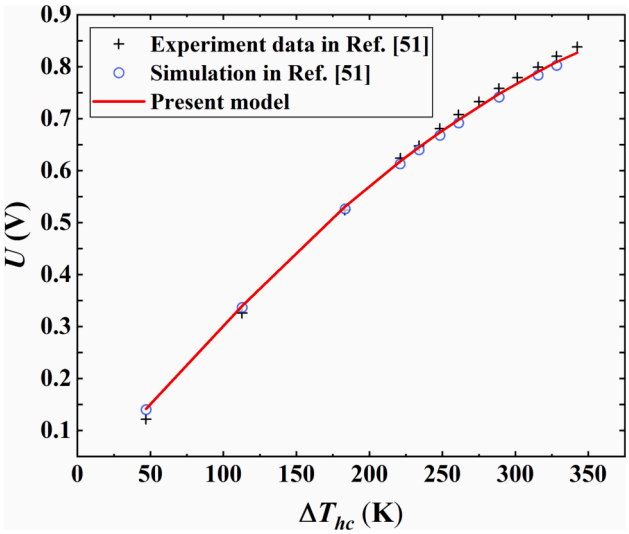

Fig. 5. Model validation with experimental data and simulations.

Under isothermal conditions, when the thermal resistance of the ATEG substrate layer (denoted as ω) is neglected (ω tends to 0), Eqs. (19) and (20) suggest that $m_{opt}(P_{max}) = 1$ and $m_{opt}(\eta_{max})=\sqrt{1+ZT}$, which aligns with the findings of Ref. [54]. However, considering the importance of the substrate layer, its thermal resistance cannot be disregarded. Fig. 6(c) illustrates $m_{opt}(P_{max})$ and $m_{opt}(\eta_{max})$ for different Ths values. It can be observed that at various temperatures, the optimal load ratio for P_{max} is approximately 1.05, while for η_{max}, it initially increases and then decreases. Both $R_{L,opt}(P_{max})$ and $R_{L,opt}(\eta_{max})$ increase with an increase in the heat source temperature.

To demonstrate the deviation of optimal thermoelectric performance from $m = 1$, P_0 and η_0 are defined as the power and efficiency when $m = 1$. $P(m_{opt})$ and $\eta(m_{opt})$ represent the power and efficiency when thermal-electrical impedance matching is achieved. Fig. 6(d) shows $P(m_{opt})/P_0$ and $\eta(m_{opt})/\eta_0$ for different T_{hs}. The results indicate that $P(m_{opt})/P_0$ is nearly equal to 1 at different temperatures, while $\eta(m_{opt})/\eta_0$ is less than 1.046. This suggests that under isothermal boundary conditions, $m = 1$ can approximate the maximum output power. However, in practical applications, achieving isothermal conditions for thermoelectric devices is challenging due to significant thermal resistances between the ATEG and the heat source or cooler. These resistances include convective heat transfer resistance, contact thermal resistance, and contact electrical resistance.

4.1.2. Convective boundary condition

Similar to the isothermal boundary conditions, Fig. 7(a) and (b) present the *U-I*, *P-I* and *η-I* curves at different convective heat transfer coefficients, assuming the same convective heat transfer resistance at the hot and cold sides, i.e., $h = h_h = h_c$. However, due to different areas of the substrate layer at the hot and cold ends ($K_h^{-1} \neq K_c^{-1}$), it can be observed that h significantly impacts the electrical performance of the ATEG. With increasing h, both power and efficiency continuously increase, albeit with diminishing increments.

Fig. 7(c) illustrates the optimal load ratio $m_{opt}(P_{max})$ and $m_{opt}(\eta_{max})$ at different h, along with the corresponding optimal load resistances $R_{L,opt}(P_{max})$ and $R_{L,opt}(\eta_{max})$. As h increases from 10^2 W/(m^{2}K) to 10^5 W/(m^{2}K), $m_{opt}(P_{max})$ decreases from 2.02 to 1.05, $m_{opt}(\eta_{max})$ decreases from 2.11 to 1.5, and $R_{L,opt}(P_{max})$ and $R_{L,opt}(\eta_{max})$ decrease from 90 mΩ and 94 mΩ to 47 mΩ and 68 mΩ, respectively. If h continues to increase, the optimal parameters tend to approach the isothermal boundary conditions.

To demonstrate the improvement in thermoelectric performance achieved through impedance matching compared to $m = 1$ under convective conditions, $P(m_{opt})/P_0(\eta(m_{opt})/\eta_0)$ are defined as the ratio of power (efficiency) at thermal-electrical impedance matching to that at $m = 1$, as shown in Fig. 7(d). When $P(m_{opt})/P_0$ or $\eta(m_{opt})/\eta_0$ is>1, the electrical performance after impedance matching surpasses that before impedance matching. From the figure, it can be observed that m_{opt} determined by Eqs. (19) and (20) consistently enhances the power and efficiency of the ATEG compared to $m = 1$ at different h, yielding improvements of up to 15.5 % and 15.7 %, respectively. As h increases, $P(m_{opt})/P_0$ or $\eta(m_{opt})/\eta_0$ approach 1.

4.2. Influence of asymmetric parameters

The asymmetric parameter of the ATEG, γ, is defined as $\gamma = \alpha_P/\alpha_N$,

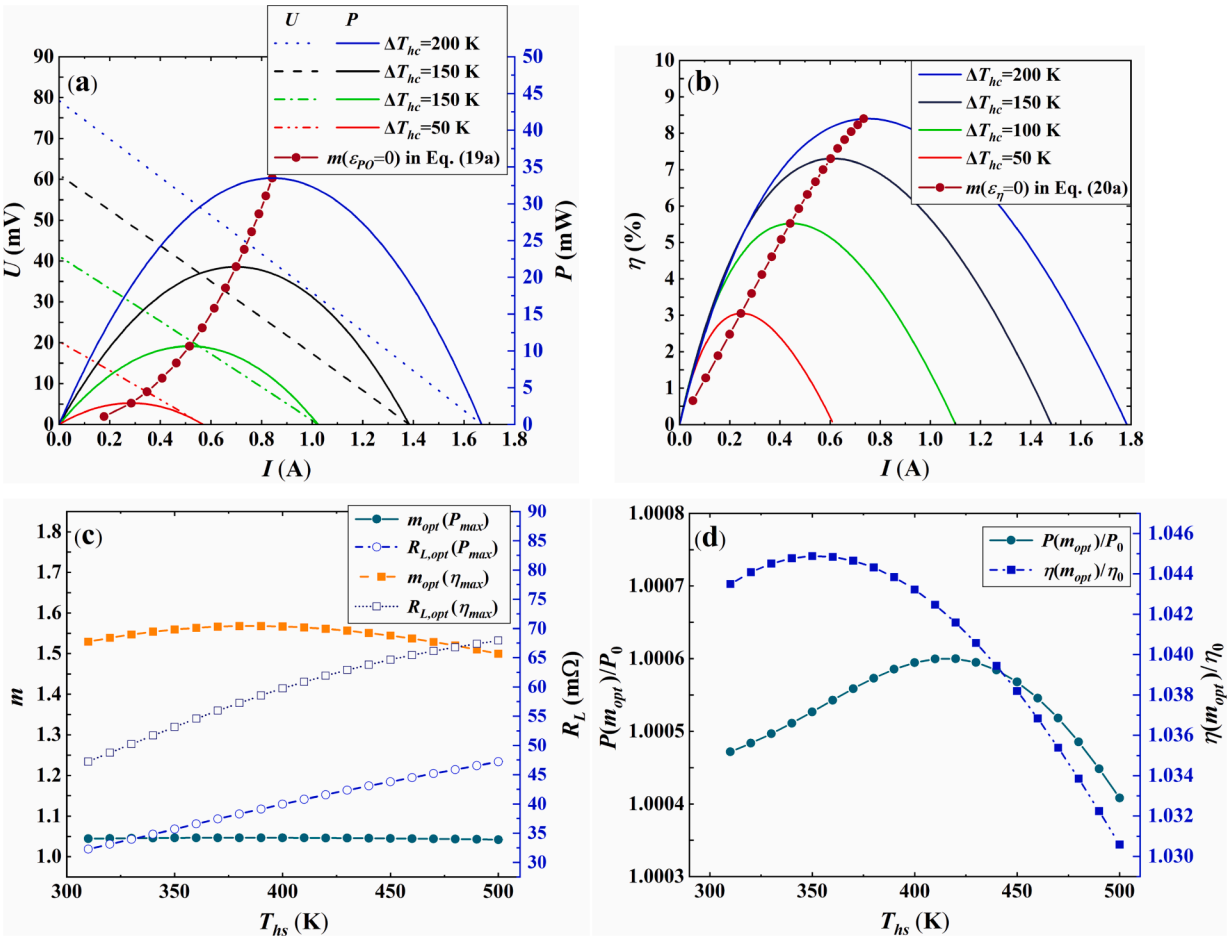

Fig. 6. Electrical properties of ATEG under boundary conditions of constant temperature. (a) $U-I$ and $P-I$ relationships, (b) $\eta-I$ relationship, (c) m_{opt} and $R_{L,opt}$ for power and efficiency, and (d) $P(m_{opt})/P_0$ and $\eta(m_{opt})/\eta_0$.

taking into account the overall volume of the asymmetric structure to match that of the symmetric configuration. This is achieved by imposing a constraint: $\alpha_P^{-1} + \alpha_N^{-1} = 2\alpha_0^{-1}$, where α_0 represents the basic parameters in Table 1. In the subsequent study and analysis, m is set according to Eq. (19) to achieve thermal-electrical impedance matching under various boundary and structural conditions.

Fig. 8(a) illustrates the impact of γ on the thermoelectric performance of the ATEG at different h. It can be observed that the output power initially increases and then decreases with increasing γ, indicating the presence of an optimal γ value for achieving maximum power output at different h. The efficiency follows a similar trend. The extremum points of the P-γ and η-γ curves occur at $\gamma < 1$, highlighting the superior thermoelectric performance of the asymmetrical ATEG. Moreover, as h increases, $\gamma_{opt}(P_{max})$ and $\gamma_{opt}(\eta_{max})$ also increase.

To determine the optimal asymmetric structure under different boundary conditions, the values of γ_{opt} targeting P_{max} and η_{max} are determined using Eq. (24). Fig. 8(b) and (c) present the γ_{opt} values (along with the corresponding P_{max} and η_{max}) under different convective conditions, considering various temperature differences between the hot and cold source (ΔT_{hc}). The results indicate that for $\Delta T_{hc} = 200$ K, $\gamma_{opt}(P_{max})$ increases from approximately 0.4 to 0.7 as h increases. When ΔT_{hc} decreases to 50 K, the range of variation for γ_{opt} expands to approximately 0.35——0.75. Similarly, the range of variation for $\gamma_{opt}(\eta_{max})$ increases as ΔT_{hc} decreases. It is important to note that under various boundary conditions, γ_{opt} is consistently less than 1, indicating that the P-legs are always thinner than the N-legs to achieve optimal thermoelectric performance. This observation is attributed to the combined effects of resistances, thermal conductivity, and substrate layer characteristics of the P-legs and N-legs, as expressed in Eq. (24).

To quantitatively analyze the performance advantages of asymmetrical ATEGs, Fig. 8(d) presents $P(\gamma_{opt})/P_0$ and $\eta(\gamma_{opt})/\eta_0$ under different boundary conditions, where P_0 and η_0 represent the power and efficiency, respectively, at $\gamma = 1$. Both $P(\gamma_{opt})/P_0$ and $\eta(\gamma_{opt})/\eta_0$ decrease as h increases, converging to approximately 1.02 and 1.045, respectively. This indicates that under both constant temperature and convective conditions, asymmetrical ATEGs outperform symmetrical ATEGs. In comparison to symmetric structures, asymmetric structures can achieve improvements in power and efficiency of up to 13.8 % and 14 %, respectively.

For the ring-shaped PN legs, the inner radius r_h needs to be designed according to different heat source sizes to accommodate the cylindrical heat exchanger [54]. To examine the combined effect of r_h and L_{leg} on the asymmetric structure, Fig. 9 presents contour plots of the ATEG power output and optimal asymmetric parameters for different r_h and L_{leg} values under convective boundary conditions with $h = 1000$ W/(m^{2}K). According to the figure, r_h has a minor impact on γ_{opt}, but an increase in r_h positively affects γ_{opt} when L_{leg} is relatively large. γ_{opt} is highly sensitive to L_{leg}, and it increases from 0.4 to 0.68 as L_{leg} increases. As depicted in Fig. 9(b), the power initially increases and then decreases with an increase in L_{leg}, with an optimal L_{leg} of 2.5 mm for different r_h. Furthermore, increasing r_h helps improve Power because, as indicated by Eq. (15), increasing r_h reduces ω, and according to Eq. (17), it decreases the leg thermal conductance K_{leg} and external thermal resistance K_{ex}^{-1}, thereby enhancing the power.

In practical applications, it is common to encounter asymmetric thermal convection conditions at both ends of the ATEG [55]. To

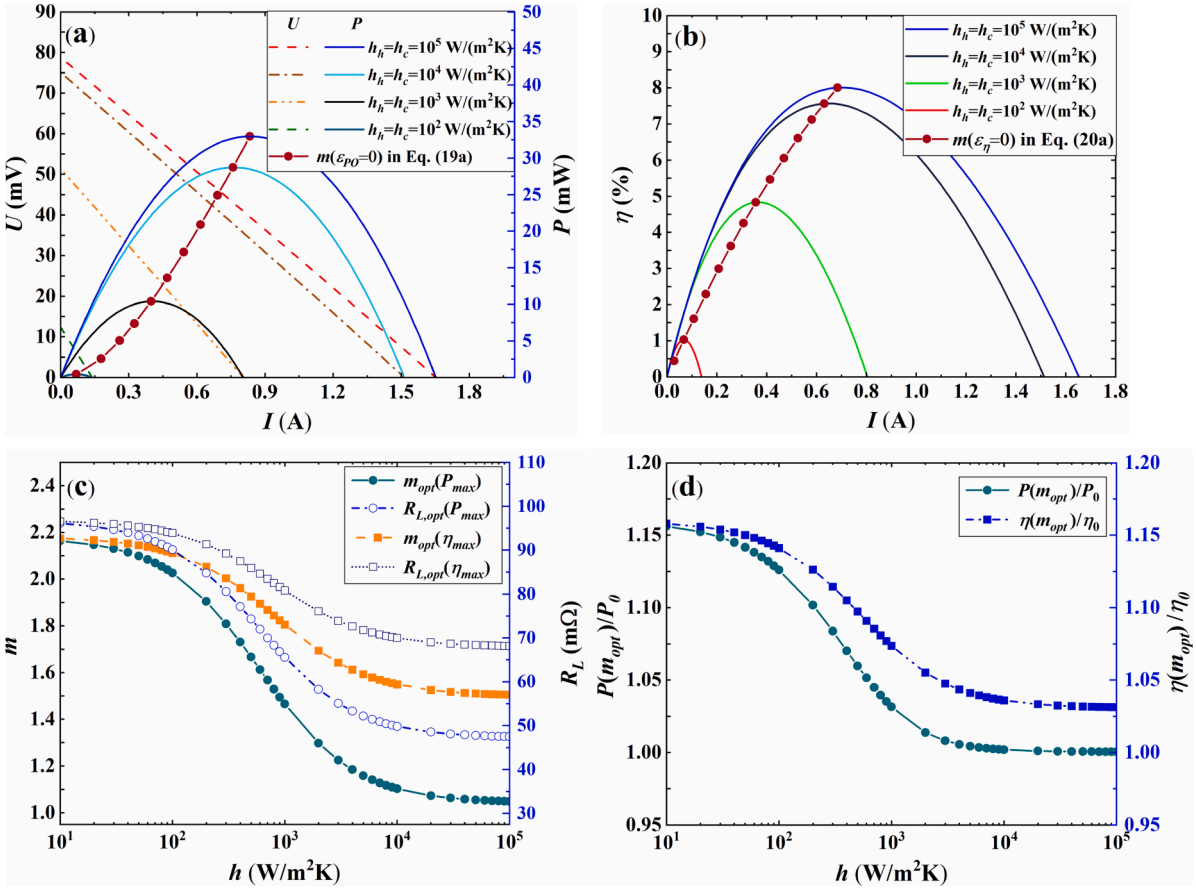

Fig. 7. Electrical properties of ATEG for convective boundary conditions. (a) $U-I$ and $P-I$ relationships, (b) $\eta-I$ relationship, (c) m_{opt} and $R_{L,opt}$ for power and efficiency, and (d) $P(m_{opt})/P_0$ and $\eta(m_{opt})/\eta_0$.

examine the thermal-electric performance of the asymmetrical ATEG under such conditions, the total convective thermal resistance $h_t^{-1} = h_h^{-1} + h_c^{-1}$ is initially set, and $h_r = h_h/h_c$ is defined to represent the degree of asymmetry in convective heat transfer at both ends of the ATEG. Moreover, utilizing the equations derived in Eq. (26), the structural parameter α and the asymmetric parameter γ of the ATEG are optimized simultaneously. Fig. 10(a) illustrates the impact of h_r on γ_{opt} and m_{opt} for different h_t. γ_{opt} increases as h_r increases, while m_{opt} exhibits the opposite trend. It is important to note that when h_r approaches 1, the impact of h_t on γ_{opt} and m_{opt} is minimal. This can be attributed to γ_{opt} being independent of K_{ex}^{-1}, as stated in Eq. (26).

Fig. 10(b) demonstrates the influence of h_r on P and α_{opt} for different ΔT_{hc}, with $h_t = 10^3$ W/(m^{2}K). For $\Delta T_{hc} = 200$ K, P decreases with an increase in h_r, while it slightly increases for $\Delta T_{hc} = 100$ K and 50 K. It is evident that under a significant temperature difference between the hot and cold sources, improving h_h leads to superior thermal-electric performance compared to enhancing the cooling capability on the cold side. However, when the temperature difference is small, directing efforts towards improving the cooling capability on the cold side can slightly enhance the thermal-electric performance. Furthermore, under different ΔT_{hc}, γ_{opt} decreases as h_r increases. Once α_{opt} and γ_{opt} are determined for specific boundary conditions, $\Delta\varphi\delta$ can be determined by fixing r_h and L_{leg}.

4.3. Thermomechanical analysis of asymmetrical ATEG with Comsol

It is crucial to investigate the local temperature distribution and thermomechanical performance of the asymmetrical ATEG to ensure its thermal reliability is not compromised. Utilizing the established analytical optimization model, once the inner arc radius and leg length of the ATEG are determined (e.g., $r_h = 20$ mm and $L_{leg} = 2.5$ mm), the optimal values of $\gamma_{opt}(P_{max})$ and $\alpha_{opt}(P_{max})$ can be obtained using Eq. (26). Subsequently, by performing simple calculations, the corresponding structural parameters of the P-type and N-type legs can be derived, as presented in Table 3. To showcase the superior electrical and thermal performance of the asymmetric structure, a symmetrical ATEG is established as a control group. To maintain control over variables, the PN leg volumes of both the symmetric and asymmetric structures are kept identical. Furthermore, a three-dimensional thermomechanical model of the ATEG under both structures is constructed in Comsol. The convection boundary conditions are set as $h_h = h_c = h = 1000$ W/(m^{2}K), $T_{hs} = 500$ K, and $T_{cs} = 300$ K.

Fig. 11 presents a comparison of the temperature distribution, Seebeck potential distribution, and leg thermal stress distribution contour maps between the symmetrical and asymmetrical ATEGs under identical convection boundary conditions. From Fig. 11(a) and (d), it can be observed that the temperature difference of the symmetrical legs is 99 K, while the temperature difference of the asymmetrical legs is 106 K, representing a 7 % increase. The presence of asymmetrical annular legs leads to an elevation in temperature at the hot end and a reduction in temperature at the cold end. This effect is attributed to the asymmetric structure, which decreases the overall thermal conductivity of the ATEG. Examining Fig. 11(b) and (e) reveals that the Seebeck voltage of the asymmetrical ATEG increases by 1.84 mV. Simple calculations indicate that the output power of the ATEG improves from 11.16 mW in the symmetric structure to 12.97 mW, resulting in a remarkable 16.2 % enhancement.

Fig. 11(c) and (f) illustrate the von Mises stress contour maps for both ATEG configurations. The maximum thermal stress in the ATEG is observed on the surface of the hot side in contact with the copper

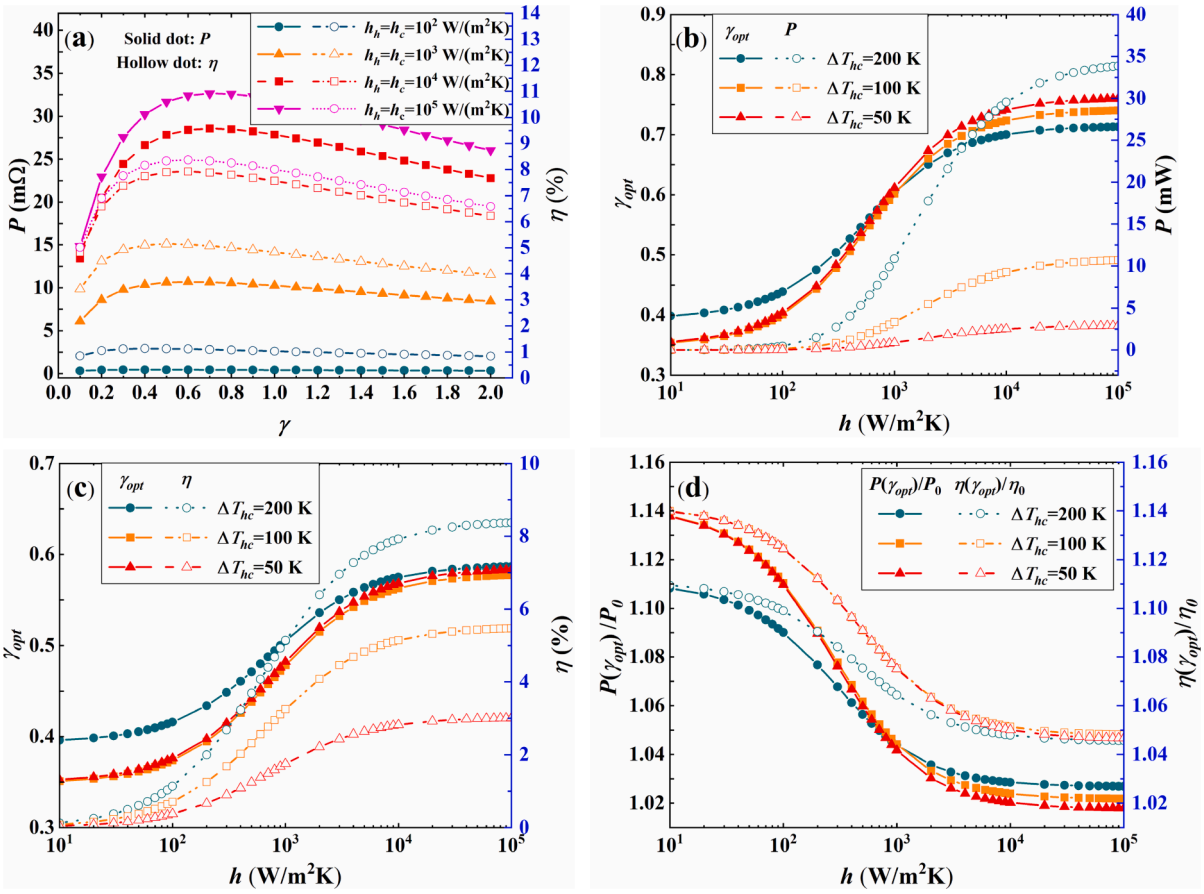

Fig. 8. (a) P and η versus γ; (b) γ_{opt} and the maximum P, (c) γ_{opt} and the maximum η under different h; (d) $P_{m,opt}/P_0$ and $\eta_{m,opt}/\eta_0$ versus h under different ΔT_{hc}.

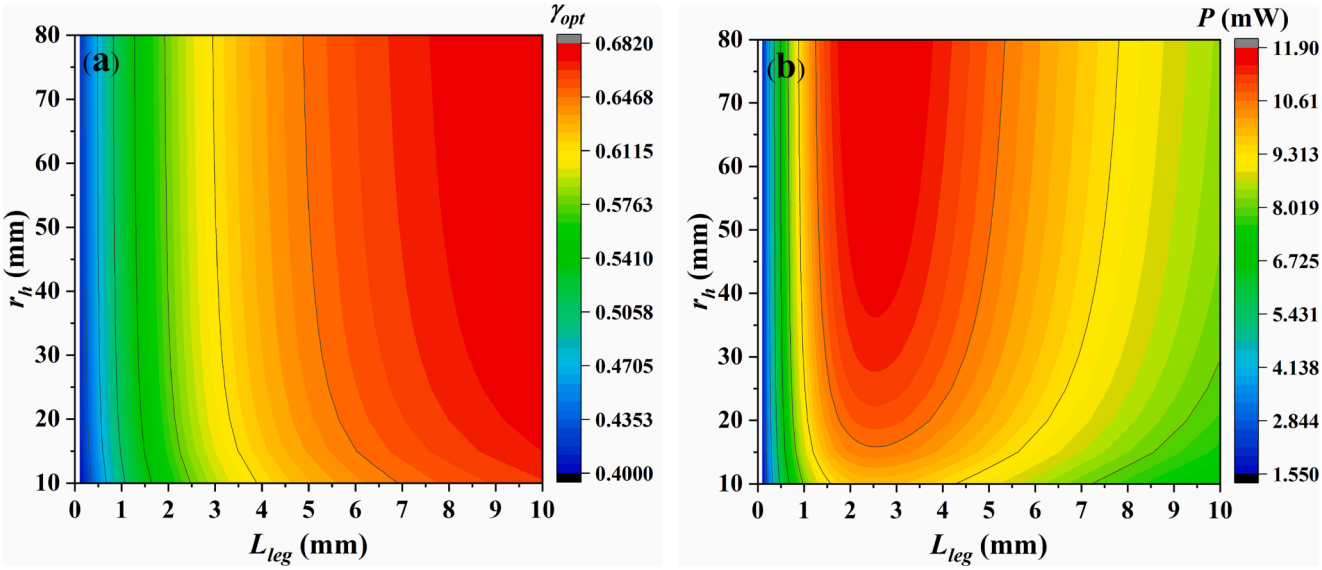

Fig. 9. The contour map of (a) optimal asymmetric parameters and (b) power output for different r_h and L_{leg} under convective boundary conditions with h = 1000 W/(m^{2}K).

interconnects. Typically, this maximum thermal stress is found around the edges of the legs. In the case of asymmetrical legs, the maximum thermal stress reaches 185.92 MPa due to the increased temperature at the hot end, resulting in larger thermal stresses when exposed to significant temperature gradients. Although the asymmetric structure reduces thermal reliability, the maximum thermal stress remains comparable to that of the segmented ATEG proposed in Ref. [56]. Furthermore, in comparison to the variable-angle ATEG proposed by Weng et al. [42], the asymmetrical ATEG exhibits higher mechanical reliability.

In practical scenarios, the operating conditions of an ATEG can vary due to external factors. Thus, an ATEG designed as the optimal

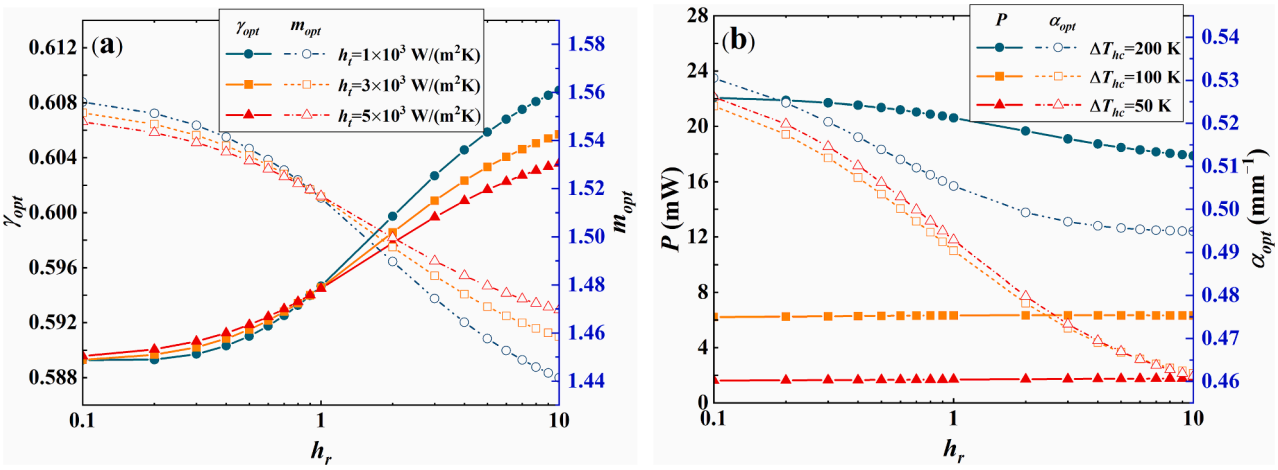

Fig. 10. Impact of h_r on optimal parameters. (a) Influence of h_r on γ_{opt} and m_{opt} for different h_t. (b) Influence of h_r on α_{opt} and P for different ΔT_{hc}.

Table 3
Optimal ATEG structure parameters.

Configuration	$m_{opt}(P_{max})$	$\gamma_{opt}(P_{max})$	$\alpha_{p,opt}(P_{max})$	$\Delta\varphi$	δ	$R_{L,opt}$
Asymmetrical ATEG	1.516	0.5947	953.438 m^{-1}	$\Delta\varphi_{p,opt}=4.34°$, $\Delta\varphi_{n,opt}=3.35°$	$\delta_{p,opt}=1.629$ mm, $\delta_{n,opt}=1.256$ mm	0.056 Ω
symmetrical ATEG	1.516	1	1196.4 m^{-1}	$\Delta\varphi_p=\Delta\varphi_n=3.88°$	$\delta_p=\delta_n=1.454$ mm	0.0607 Ω

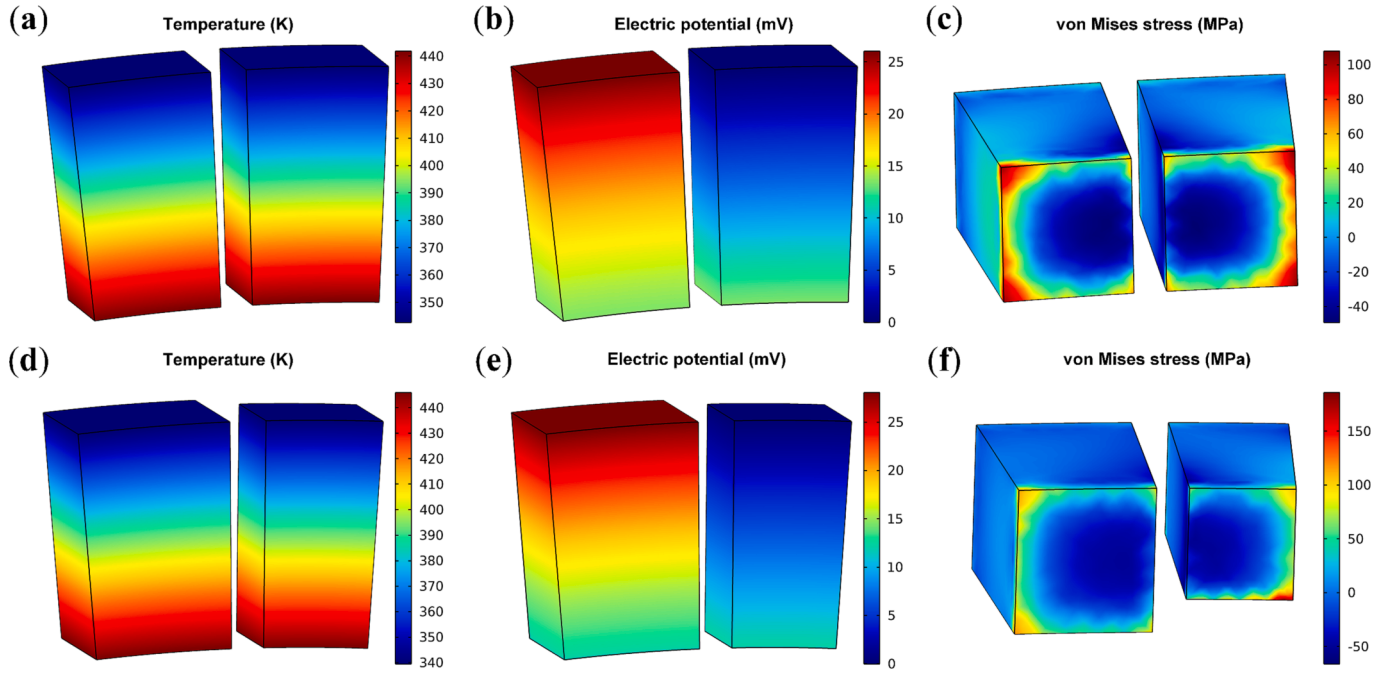

Fig. 11. Contour maps of ATEG properties. (a) Temperature distribution, (b) Seebeck potential distribution, and (c) leg thermal stress distribution of symmetrical ATEG; (d) Temperature distribution, (e) Seebeck potential distribution, and (f) leg thermal stress distribution of asymmetrical ATEG.

asymmetric structure for a specific set of boundary conditions may encounter different thermal boundary conditions during operation. To assess the thermal reliability of the asymmetrical ATEG under such variations, Figs. 12 and 13 depict the thermal stress distribution maps of the optimal asymmetrical ATEG structures obtained from Table 3 under asymmetric thermal boundary conditions. The figures reveal that the maximum thermal stress in the asymmetrical ATEG increases as h_r (the degree of asymmetry) increases.

In the case of $h_t = 500$ W/(m^{2}K), as depicted in Fig. 12, the maximum thermal stress in the ATEG rises from 147.38 MPa at $h_r = 0.1$ to 230.62 MPa at $h_r = 10$. These findings suggest that improving the heat transfer between the ATEG and the cooler leads to greater mechanical reliability compared to enhancing the heat transfer between the ATEG and the heat source.

Similarly, for $h_t = 1000$ W/(m^{2}K) shown in Fig. 13, the maximum thermal stress in the ATEG increases from 189.68 MPa at $h_r = 0.1$ to 241.04 MPa at $h_r = 10$. Comparing Fig. 12 and Fig. 13, it can be observed that reducing the overall convective thermal resistance can partially alleviate the negative impact of asymmetric thermal boundary conditions on the mechanical reliability of the legs.

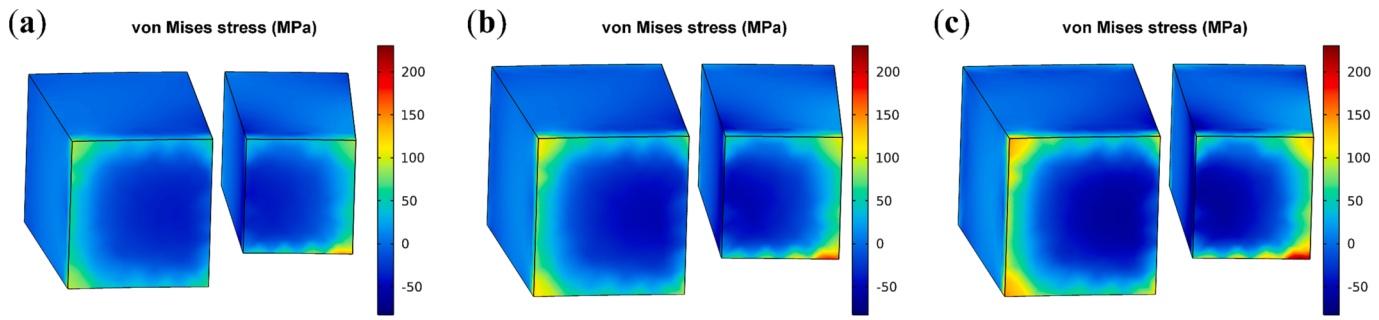

Fig. 12. Thermal stress distribution of asymmetrical ATEG under different h_r with h_t = 500 W/(m^{2}K): (a) h_r = 0.1, (b) h_r = 1, and (c) h_r = 10.

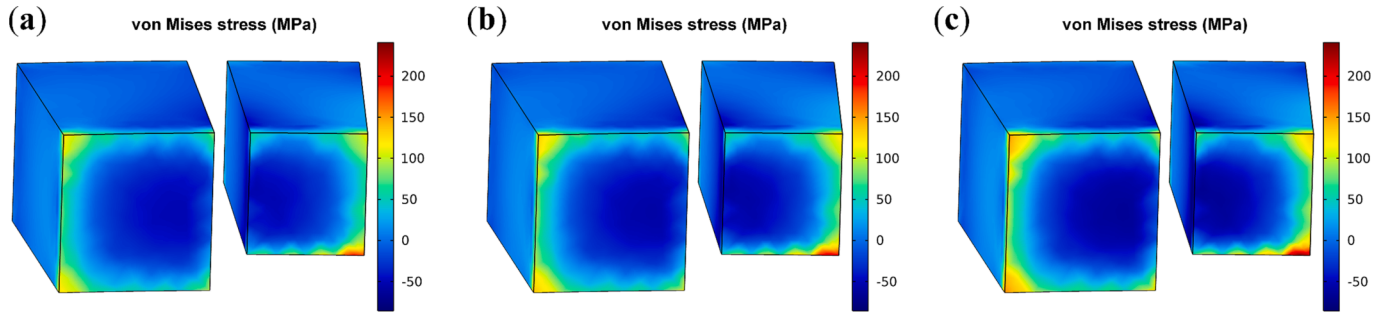

Fig. 13. Thermal stress distribution of asymmetrical ATEG under different h_r with h_t = 1000 W/(m^{2}K): (a) h_r = 0.1, (b) h_r = 1, and (c) h_r = 10.

5. Conclusions

An asymmetrical annular thermoelectric generator is proposed, where distinct structural parameters are configured for the P-type and N-type legs to balance the impact of different thermoelectric materials' resistivity and thermal conductivity on the thermal properties of the ATEG. A comprehensive analysis model of asymmetrical ATEG is established, including load matching model and asymmetric coefficient optimization model. The load ratio m, annular leg structural parameter α, and asymmetry parameter γ are defined and the thermal-electrical impedance matching conditions of ATEG under different boundary conditions are studied. The influence of thermal boundary conditions on the optimal structural parameters of asymmetrical ATEGs is analyzed. Based on the obtained optimal asymmetric parameters, a three-dimensional numerical model is established to analyze the thermal reliability of the ATEG. The main findings of this study are:

(1) After achieving thermal-electrical impedance matching, power and efficiency can be improved by approximately 15 % under convective conditions.
(2) Compared with conventional ATEG, the output power of asymmetrical ATEG can be increased by about 16.2 % for the same material volume. To achieve better thermoelectric performance, the volume of the P-type leg is consistently greater than that of the N-type leg under different boundary conditions.
(3) Increasing the ratio of convective heat transfer coefficients between the hot and cold sides, h_r, can increase the optimal asymmetric parameter γ_{opt} and reduce the optimal load ratio m_{opt}, but it has a relatively small impact on the output power.
(4) The introduction of the asymmetric structure increases the maximum thermal stress on the legs while increasing the temperature difference, which means that improving electrical performance comes at the expense of mechanical reliability.
(5) As h_r increases from 0.1 to 10, the maximum thermal stress increases from 147.38 MPa to 230.62 MPa. Reducing the thermal resistance between the ATEG and the heat sink proves to be more effective in enhancing mechanical reliability compared to reducing the thermal resistance between the ATEG and the heat source.

Declaration of Competing Interest

The authors declare that they have no known competing financial interests or personal relationships that could have appeared to influence the work reported in this paper.

Data availability

Data will be made available on request.

Acknowledgment

This research was funded by the National Natural Science Foundation of China (51977164).

References

[1] H. He, F. Sun, Z. Wang, C. Lin, C. Zhang, R. Xiong, et al., China's battery electric vehicles lead the world: achievements in technology system architecture and technological breakthroughs, Green Energy Intell. Transp. 1 (2023), 100020.
[2] A.O. Ochieng, T.F. Megahed, S. Ookawara, H. Hassan, Comprehensive review in waste heat recovery in different thermal energy-consuming processes using thermoelectric generators for electrical power generation, Process Saf. Environ. 162 (2022) 134–154.
[3] W. Yang, W. Zhu, B. Du, H. Wang, L. Xu, C. Xie, et al., Power generation of annular thermoelectric generator with silicone polymer thermal conductive oil applied in automotive waste heat recovery, Energy 282 (2023), 128400.
[4] D. Luo, Z. Wu, Y. Yan, D. Ji, Z. Cheng, R. Wang, et al., Optimal design of a heat exchanger for automotive thermoelectric generator systems applied to a passenger car, Appl. Therm. Eng. 227 (2023), 120360.
[5] Y. Liu, Y. Zhang, Q. Xiang, F. Hao, Q. An, H. Chen, Comprehensive modeling and parametric analysis of Multi-Mission Radioisotope Thermoelectric Generator, Appl. Therm. Eng. 219 (2023), 119447.
[6] M.N. Hasan, N. Nayan, M. Nafea, A.G. Muthalif, M.S.M. Ali, Novel structural design of wearable thermoelectric generator with vertically oriented thermoelements, Energy 259 (2022), 125032.
[7] Y. Maleki, F. Pourfayaz, M. Mehrpooya, Experimental study of a novel hybrid photovoltaic/thermal and thermoelectric generators system with dual phase change materials, Renew. Energy 201 (2022) 202–215.

[8] N. Kuang, Z. Zuo, W. Wang, R. Liu, High performance flexible thin-film thermoelectric generator heated by methanol catalytic combustion, Appl. Therm. Eng. 219 (2023), 119346.
[9] D. Yuan, W. Jiang, A. Sha, J. Xiao, J. Shan, D. Wang, Energy output and pavement performance of road thermoelectric generator system, Renew. Energy 201 (2022) 22–33.
[10] T. Sun, L. Wang, W. Jiang, Pushing thermoelectric generators toward energy harvesting from the human body: challenges and strategies, Mater. Today 57 (2022) 121–145.
[11] L. Xie, J. Yang, Z. Liu, N. Qu, X. Dong, J. Zhu, et al., Highly efficient thermoelectric cooling performance of ultrafine-grained and nanoporous materials, Mater. Today 65 (2023) 5–13.
[12] C. Zhou, Y.K. Lee, Y. Yu, S. Byun, Z.-Z. Luo, H. Lee, et al., Polycrystalline SnSe with a thermoelectric figure of merit greater than the single crystal, Nat. Mater. 20 (2021) 1378–1384.
[13] R. Sok, J. Kusaka, Experimental and modeling analysis on thermoelectric heat recovery to maximize the performance of next-generation diesel engines dedicated for future electrified powertrains, Appl. Therm. Eng. 219 (2023), 119530.
[14] F. Tohidi, S. Ghazanfari Holagh, A. Chitsaz, Thermoelectric generators: a comprehensive review of characteristics and applications, Appl. Therm. Eng. 201 (2022), 117793.
[15] A. Montecucco, K. Siviter, A.R. Knox, The effect of temperature mismatch on thermoelectric generators electrically connected in series and parallel, Appl. Energy 123 (2014) 47–54.
[16] I.R. Cózar, T. Pujol, M. Lehocky, Numerical analysis of the effects of electrical and thermal configurations of thermoelectric modules in large-scale thermoelectric generators, Appl. Energy 229 (2018) 264–280.
[17] T. Choi, T.Y. Kim, Three-zone numerical modeling method for predicting system-level waste heat recovery performance of thermoelectric generator with various electrical array configurations, Energ. Conver. Manage. 240 (2021), 114270.
[18] B. Bijukumar, A.G. Kaushik Raam, V. Sukanya, C.M. Nirmal Mukundan, A. Al-Durra, Investigation on arrangement of thermoelectric modules based on exhaust gas flow direction to minimize mismatch power loss in TEG arrays, Appl. Therm. Eng. 221 (2023), 119853.
[19] D. Luo, R. Wang, W. Yu, W. Zhou, Performance optimization of a converging thermoelectric generator system via multiphysics simulations, Energy 204 (2020), 117974.
[20] W.-H. Chen, C.-M. Wang, L.H. Saw, A.T. Hoang, A.A. Bandala, Performance evaluation and improvement of thermoelectric generators (TEG): Fin installation and compromise optimization, Energ. Conver. Manage. 250 (2021), 114858.
[21] W.-H. Chen, Y.-B. Chiou, R.-Y. Chein, J.-Y. Uan, X.-D. Wang, Power generation of thermoelectric generator with plate fins for recovering low-temperature waste heat, Appl. Energy 306 (2022), 118012.
[22] J.-H. Meng, Y. Liu, X.-H. Zhu, Z.-J. Yang, K. Zhang, G. Lu, Performance enhancement for exhaust thermoelectric power generation system by using porous pin fins based on a fully automatic optimization method, Energ. Conver. Manage. 273 (2022), 116404.
[23] W. Yang, W. Zhu, Y. Li, L. Zhang, B. Zhao, C. Xie, et al., Annular thermoelectric generator performance optimization analysis based on concentric annular heat exchanger, Energy 239 (2022), 122127.
[24] W. Zhu, A. Xu, W. Yang, B. Xiong, C. Xie, Y. Li, et al., Optimal design of annular thermoelectric generator with twisted tape for performance enhancement, Energ. Conver. Manage. 270 (2022), 116258.
[25] Y. Li, S. Wang, Y. Fu, Y. Zhao, L. Yue, Influence of foamed metal core flow heat transfer enhancement on the performance of thermoelectric generators with different power generation characteristics, Therm. Sci. Eng. Prog. 31 (2022), 101300.
[26] Y. Zhao, M. Lu, Y. Li, M. Ge, L. Xie, L. Liu, Characteristics analysis of an exhaust thermoelectric generator system with heat transfer fluid circulation, Appl. Energy 304 (2021), 117896.
[27] N. Pacheco, F.P. Brito, R. Vieira, J. Martins, H. Barbosa, L.M. Goncalves, Compact automotive thermoelectric generator with embedded heat pipes for thermal control, Energy 197 (2020), 117154.
[28] Y. Tian, A. Liu, J. Wang, Y. Zhou, C. Bao, H. Xie, et al., Optimized output electricity of thermoelectric generators by matching phase change material and thermoelectric material for intermittent heat sources, Energy 233 (2021), 121113.
[29] B.-H. Hong, Z.-Y. Zhou, X.-Y. Huang, J.-W. He, Y. Cai, W.-W. Wang, et al., A comprehensive investigation of PCM based annular thermoelectric generator for energy recovery: energy conversion characteristics and performance evaluation, Appl. Therm. Eng. 228 (2023), 120474.
[30] Z. Zhao, Z. Zuo, W. Wang, R. Liu, N. Kuang, Performance optimization for a combustion-based micro thermoelectric generator with two-stage thermoelectric module, Appl. Therm. Eng. 198 (2021), 117464.
[31] C. Maduabuchi, C. Eneh, A.A. Alrobaian, M. Alkhedher, Deep neural networks for quick and precise geometry optimization of segmented thermoelectric generators, Energy 263 (2023), 125889.
[32] Y. Ge, K. He, L. Xiao, W. Yuang, S.-M. Huang, Geometric optimization for the thermoelectric generator with variable cross-section legs by coupling finite element method and optimization algorithm, Renew. Energy 183 (2022) 294–303.
[33] H.-B. Liu, J.-H. Meng, X.-D. Wang, W.-H. Chen, A new design of solar thermoelectric generator with combination of segmented materials and asymmetrical legs, Energ. Conver. Manage. 175 (2018) 11–20.
[34] D.R. Karana, R.R. Sahoo, Influence of geometric parameter on the performance of a new asymmetrical and segmented thermoelectric generator, Energy 179 (2019) 90–99.
[35] W.-H. Chen, T.-H. Huang, G.L. Augusto, R. Lamba, C. Maduabuchi, L.H. Saw, Power generation and thermal stress characterization of thermoelectric modules with different unileg couples by recovering vehicle waste heat, J. Clean. Prod. 375 (2022), 133987.
[36] Z.-G. Shen, B. Huang, X. Liu, Effect of structure parameters on the performance of an annular thermoelectric generator for automobile exhaust heat recovery, Energ. Conver. Manage. 256 (2022), 115381.
[37] W. Yang, W. Zhu, Y. Li, C. Xie, B. Xiong, Y. Shi, et al., Global structural optimization of annular thermoelectric generators based on a dual-finite-element multiphysical model, Appl. Therm. Eng. 220 (2023), 119797.
[38] M. Aljaghtham, E. Celik, Energy conversion and thermal reliability of thermoelectric materials in unileg annular configuration, Mater. Lett. 300 (2021), 130192.
[39] B. Hua, I.B. Mansir, M. Alanazi, A. Alanazi, S.M. Eldin, N. Alkhamis, Economic and energy-exergy analysis of a novel in-plane solar segmented annular thermometric generator, Therm. Sci. Eng. Prog. 40 (2023), 101768.
[40] M.-W. Tian, I.B. Mansir, S.M. Eldin, H. Ayed, H. Loukil, N. Alkhamis, Economic and thermal performance analysis of two-stage thin-film solar thermoelectric power generator, Case Stud. Therm. Eng. 45 (2023), 103012.
[41] O. Caballero-Calero, M. Rull-Bravo, D. Platzek, M.D. Cárdenas, R. Fernández, A. Moure, et al., Tubular ring thermoelectric module for exhaust pipes: from Skutterudite nanopowders to the final device, Energy 234 (2021), 121223.
[42] Z. Weng, F. Liu, W. Zhu, Y. Li, C. Xie, J. Deng, et al., Performance improvement of variable-angle annular thermoelectric generators considering different boundary conditions, Appl. Energy 306 (2022), 118005.
[43] M.H. Zaher, M.Y. Adbelsalam, J.S. Cotton, Non-dimensional design optimization of annular thermoelectric generators integrated in waste heat recovery applications, Energ. Convers. Manage. 253 (2022), 115141.
[44] S. Shittu, G. Li, X. Zhao, X. Ma, Review of thermoelectric geometry and structure optimization for performance enhancement, Appl. Energy 268 (2020), 115075.
[45] S. Asaadi, S. Khalilarya, S. Jafarmadar, A thermodynamic and exergoeconomic numerical study of two-stage annular thermoelectric generator, Appl. Therm. Eng. 156 (2019) 371–381.
[46] M.-W. Tian, L.W.W. Mihardjo, H. Moria, S. Asaadi, H.S. Dizaji, S. Khalilarya, et al., A comprehensive energy efficiency study of segmented annular thermoelectric generator; thermal, exergetic and economic analysis, Appl. Therm. Eng. 181 (2020), 115996.
[47] A. Attar, H.S. Lee, G.J. Snyder, Optimum load resistance for a thermoelectric generator system, Energ. Convers. Manage. 226 (2020), 113490.
[48] Z.-Z. He, A coupled electrical-thermal impedance matching model for design optimization of thermoelectric generator, Appl. Energy 269 (2020), 115037.
[49] S.I. Kim, K.H. Lee, H.A. Mun, H.S. Kim, S.W. Hwang, J.W. Roh, et al., Dense dislocation arrays embedded in grain boundaries for high-performance bulk thermoelectrics, Science 348 (2015) 109–114.
[50] W.S. Liu, Q.Y. Zhang, Y.C. Lan, S. Chen, X. Yan, Q. Zhang, et al., Thermoelectric property studies on Cu-doped n-type $CuxBi_2Te_{2.7}Se_{0.3}$ nanocomposites, Adv. Energy Mater. 1 (2011) 577–587.
[51] D. Ebling, M. Jaegle, M. Bartel, A. Jacquot, H. Bottner, Multiphysics simulation of thermoelectric systems for comparison with experimental device performance, J. Electron. Mater. 38 (2009) 1456–1461.
[52] S. Asaadi, S. Khalilarya, S. Jafarmadar, Numerical study on the thermal and electrical performance of an annular thermoelectric generator under pulsed heat power with different types of input functions, Energ. Convers. Manage. 167 (2018) 102–112.
[53] W. Zhu, W. Yang, Y. Yang, Y. Li, H. Li, Y. Shi, et al., Economic configuration optimization of onboard annual thermoelectric generators under multiple operating conditions, Renew. Energy 197 (2022) 486–499.
[54] W. Zhu, Z. Weng, Y. Li, L. Zhang, B. Zhao, C. Xie, et al., Theoretical analysis of shape factor on performance of annular thermoelectric generators under different thermal boundary conditions, Energy 239 (2022), 122285.
[55] D. Luo, Z. Liu, Y. Yan, Y. Li, R. Wang, L. Zhang, et al., Recent advances in modeling and simulation of thermoelectric power generation, Energ. Convers. Manage. 273 (2022), 116389.
[56] S. Shittu, G. Li, X. Zhao, X. Ma, Y.G. Akhlaghi, E. Ayodele, High performance and thermal stress analysis of a segmented annular thermoelectric generator, Energ. Convers. Manage. 184 (2019) 180–193.